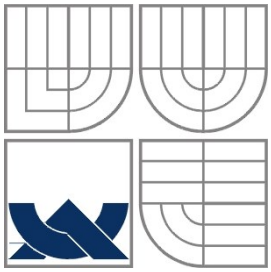

VYSOKÉ UČENÍ TECHNICKÉ V BRNĚ
BRNO UNIVERSITY OF TECHNOLOGY

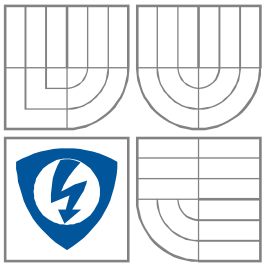

FAKULTA ELEKTROTECHNIKY A KOMUNIKAČNÍCH TECHNOLOGIÍ
ÚSTAV RADIOELEKTRONIKY

FACULTY OF ELECTRICAL ENGINEERING AND COMMUNICATION
DEPARTMENT OF RADIOELECTRONICS

ADVANCED ALGORITHMS FOR SATELLITE COMMUNICATION SIGNAL PROCESSING

POKROČILÉ ALGORITMY ZPRACOVÁNÍ SIGNÁLŮ PRO DRUŽICOVOU KOMUNIKACI

DIZERTAČNÍ PRÁCE
DOCTORAL THESIS

AUTOR PRÁCE — Ing. FILIP ZÁPLATA
AUTHOR

VEDOUCÍ PRÁCE — prof. Ing. MIROSLAV KASAL, CSc.
SUPERVISOR

BRNO, 2015

Keywords

Software defined radio, digital signal processing, satellite communication, deep-space communication, digital downconversion, multirate filtration, undersampling, Goertzel algorithm, frequency estimation, Doppler shift, MATLAB Simulink.

Klíčová slova

Softwarově definované rádio, číslicové zpracování signálu, družicová komunikace, komunikace s hlubokým vesmírem, číslicová downkonverze, filtrace s více vzorkovacími kmitočty, podvzorkování, Goertzelův algoritmus, synchronizace nosné, Dopplerův posuv, MATLAB Simulink.

Contents

1. Introduction 1

2. Objectives of the thesis 2

3. Downconversion of narrowband signals 2

3.1. Novel approach to digital downconversion 3

3.1.1. Low speed digital AM signal detection 4

3.1.2. Goertzel filter composition 5

3.1.3. Goertzel filter modification for real frequency 6

3.1.4. Improved structure of the decimating filter 8

3.2. Digital downconverter performance 12

3.2.1. BER influence 12

3.2.2. Computational demands 14

3.2.3. Quantization errors of the algorithms 15

3.3. Simulink tests 16

3.3.1. BERtool models 16

3.3.2. BER simulation results 17

4. Carrier synchronization 19

4.1. Frequency estimation 19

4.1.1. Spectrum averaging frequency estimator 19

4.1.2. Closed loop spectrum averaging frequency estimator 21

4.1.3. Modified closed loop spectrum averaging frequency estimator 21

4.2. Simulink tests 22

4.2.1. Spectrum averaging frequency estimator model 22

4.2.2. Estimation simulation results 24

5. Experimental tests 26

5.1. Frequency synchronization 26

5.2. Digital downconversion 28

6. Conclusion 29

7. Selected references 30

1. Introduction

Modern technology allows digitalization of signals of high bandwidths at high frequencies by powerful integrated analog to digital converters. Due to many years of work on digital signal processing, software defined radio (SDR) is becoming common nowadays. Even though its power consumption, space and technology demands are very high, compared with traditional analog technology, its benefits of reconfigurability, adaptability and algorithm abilities definitely make SDR a very perspective technology.

The SDR application is actually a program flashed into memory and run by a processing core like an ARM or some DSP, or it is a configuration file also stored in memory, but used for configuring a programmable gate array – CPLD or bigger FPGA. The processors work, sequentially, instruction by instruction and it slows their processing down, but their processing variability is vast, depending just on the flash memory space, which is mostly vastly extendable. There is a variety of processors available from general purpose microcontrollers with many integrated peripherals over specialized DSPs controlled by a very long instruction set (VLIW), including parallel processing, to GHz order speed multi-core signal processors of the highest performance able to process and put through tenths of Gbps. Programmable gate arrays, on the other hand, work with several times lower speed, but many processes are made in parallel and the processes seem to be processed in one instant. Except for its enormous processing speed and throughput, the number of gates is highly limited and the cost is still very high.

The conversion between the analog and digital domain is performed by an analog to digital converter (ADC) and a digital to analog converter (DAC), respectively. Technology in this area is also highly developed; there are many approaches to the conversion designed for specialized applications like instrumentation, audio and video applications or radio frequency processing. The sigma-delta converters provide, due to their oversampling property, the best noise performance, but the oversampling, on the other hand, does not allow high speed sampling. The integration converters are able to suppress periodic disturbances like power-line harmonic noise, and therefore are used in measurement equipment. The RF signals are converted mostly by the pipelined ADCs, because the pipelining used in this technology allows to reach the highest sampling frequencies and that of several hundreds even thousands Msps. The bandwidth of a usual signal is often many times lower, but the signal is positioned at higher frequencies. Using bandpass sampling is wise, as the need for sampling frequency depends on the signal's bandwidth instead of its frequency position. The sampler still has to be fast enough to catch the sample correctly.

Additionally, an SDR saves space on a probe and weight because of its reconfigurability for many communication standards, where the processing unit replaces blocks of analog circuits for each standard. It is even possible to make an upgrade of the whole transceiver and add or modify the communication standards. Considering extreme conditions in deep-space, there comes up questions about power consumption, heat sinking, radiation resistance, etc.

2. Objectives of the thesis

Our interests focus on the satellite communication especially at very long distances, where signal power is lost so much that noise power becomes dominant. The satellite communication must cope with large Doppler shifts of the signal frequency. The way to deal with low signal to noise ratios is slowing the communication and narrowing the occupied frequency band; the significant noise power is then usually removed by filtering. By contrast, narrowband filters makes carrier synchronization very difficult.

The objectives of the dissertation thesis are formulated as follows:

- Improve digital downconversion based on undersampling by using Fourier transform algorithms. The downconverter is supposed to be a part of a multi-rate downconversion.

The implementation of a simple mixer is straightforward and provides excellent results, but it requires to be driven by the NCO. It was presented that the implementing NCO can be a daunting task which finally makes the downconverter require many processing resources. On the contrary, the undersampling technique seems to be very effective especially for multirate downconversion. The problematic bandpass filtering would be provided by employing Fourier transform algorithms.

- Investigate the possibility of frequency synchronization based on the spectral analysis of the received signal. Focus on the narrowband signal with poor SNR and large frequency offsets.

Carrier synchronization of signals of such properties has been said to be difficult. The acquisition range of the known algorithms is too narrow to accommodate the Doppler shifts typical for satellite communication without systematically sweeping the frequency over the range. A special approach to spectrum averaging would give attractive results.

- Develop simulation models of the investigated algorithms and provide the performance analyses.

It is necessary to compare developed algorithms with existing algorithms from a performance point of view. Since the focus is aimed at digital processing, the models in MATLAB Simulink are nearly equivalent to real implementation as firmware on DSP or the configuration data for FPGA and the simulation with real input data is informative enough.

3. Downconversion of narrowband signals

In digital receivers the received signals are digitalized after analog processing (amplification, analog downconversion, filtering). Demodulation is then provided by a digital processing unit as mathematical computation. The desired signal is mostly several times oversampled and data is carried at a low intermediate frequency. Thus, the signal has to be digitally downconverted to the baseband.

3.1. Novel approach to digital downconversion

Let us have a look at the downconverter as a "black box". The input is a continuous portion of signal samples from the ADC, which contains a narrow-band signal somewhere within the sampled band among other signals, undesired ones, acting as noise. The output of the black-box is also a portion of samples, but less frequent and containing different information. Each sample is an average of the complex information contained in the selected narrow band. That is, in fact, what the discrete Fourier transform does, particularly from a selection of effective algorithms the Goertzel algorithm fits the most to such a purpose.

The derivation of the Goertzel algorithm can be found in many books, e.g. [16]. The transfer function of the Goertzel filter is

$$H(z) = \sum_{n=0}^{\infty} h(n) z^{-1} = \frac{1}{1 - z^{-1} e^{j2\pi \frac{k}{N}}}. \tag{3.1}$$

More convenient for implementing the Goertzel algorithm is the modified form

$$H(z) = \frac{1}{1 - z^{-1} e^{j2\pi \frac{k}{N}}} \cdot \frac{1 - z^{-1} e^{-j2\pi \frac{k}{N}}}{1 - z^{-1} e^{-j2\frac{k}{N}}} = \frac{1 - z^{-1} e^{-j2\pi \frac{k}{N}}}{1 - 2z^{-1} \cos\left(2\pi \frac{k}{N}\right) + z^{-2}} \tag{3.2}$$

which can be split into real recursive and complex direct computational parts.

The realization of the transfer function (3.2) is shown in Figure 3.1. Notice that the filter has two complex poles located on the unit circle which is a condition of stability.

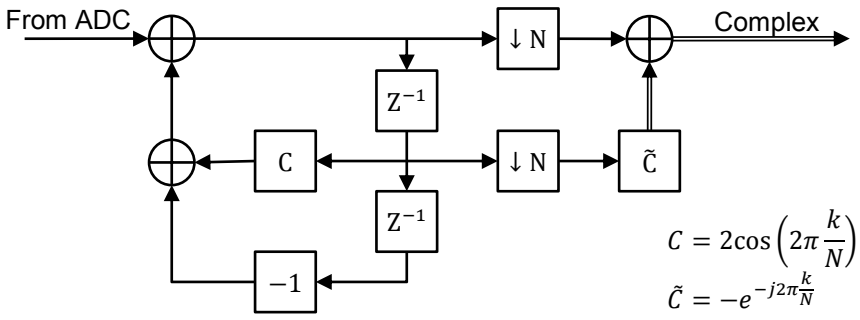

Figure 3.1: Goertzel filter as a downconverter.

The downsampling blocks are the realization of the rectangular windowing of the impulse response. The complex output is obtained by finishing by the direct part of the algorithm and is equivalent to the real and imaginary part.

By substituting $e^{j\omega}$ into the derived transfer function (3.1) we will not get the power spectral density due to the constraint of *N* samples after which the filter is reset. To get the correct frequency characteristics the inverse Fourier transform is applied to the impulse response of the Goertzel filter which, finally, yields the power spectral density

$$|H_G(f)|^2 = \frac{\sin\left(\pi N\left(\frac{k}{N} - f\right)\right)^2}{\mathrm{N}^2 \sin\left(\pi\left(\frac{k}{N} - f\right)\right)^2} \tag{3.3}$$

and the phase characteristic

$$\arg\big(H_G(f)\big) = \pi\left(\frac{k}{N} - f\right)(N-1). \tag{3.4}$$

PSD only has a one-side lobe due to the complex character of the transfer function, and the filtered signal is then, in general, also complex. The filter is tuned to a non-integer frequency, $k \in \mathbb{R}$, which is generally not possible for the discrete Fourier transform (DFT). If DFT is used, the frequency will be fixed for each bin and will depend on the length of DFT *N*. Such behavior would make DFT useless as a downconverter. Fortunately, the Goertzel algorithm may be tuned to whatever real frequency from the sampled range. When comparing the downconverter based on the CIC filter with the Goertzel downconverter in Figure 3.1 one can find that the Goertzel filter does not perform any frequency conversion in the sense of a complex mixer. Since the algorithm is able to filter the desired signal in the passband, the downconversion can be provided by downsampling as aliasing to the baseband. The technique has the restriction of the integer decimation factor *N*, which makes the Goertzel algorithm useful only as a pre-downconverter, where the final downconversion has to be performed, e.g. by the Costas loop.

The characteristics cannot be compared with the CIC-filter, first some conditions have to be applied to get desired form for comparison. The substitution the normalized frequency *f* for the angle frequency ω and assuming the desired frequency is zero yields the relation

$$|H_G(\omega)|^2\{k=0\} = \frac{1}{N^2}\frac{1-\cos(\omega N)}{1-\cos(\omega)}. \tag{3.5}$$

The Goertzel algorithm frequency characteristic is exactly the same as the CIC filter's one. Thus, the noise performance of the Goertzel downconverter will be the same.

3.1.1. Low speed digital AM signal detection

A good example of downconversion by undersampling is the DCF77 receiver published in [17]. The amplitude modulated signal expressed by

$$f_{AM}(t) = m(t)\cos(\omega_c t + \varphi_c) \tag{3.6}$$

is noticeably similar to the BPSK modulation, but the modulation function *m(t)* is generally the analog band-limited function.

In this case the conditions for the positive replica

$$\frac{2\pi}{2T_S} > \left|2\pi\frac{n}{T_S} - \omega_c\right| \Rightarrow \left|n - \frac{\omega_c T_S}{2\pi}\right| < \frac{1}{2} \tag{3.7}$$

and for the negative replica

$$\left|n + \frac{\omega_c T_S}{2\pi}\right| < \frac{1}{2} \tag{3.8}$$

has to be met. Substituting the values used in the DCF77 system to the conditions results in

$$\left| n \pm \frac{2\pi \cdot 77.5 \cdot 10^3}{2\pi \cdot 24 \cdot 10^3} \right| = |n \pm 3.23| < \frac{1}{2} \Rightarrow n = \mp 3 \tag{3.9}$$

From the values it is possible to evaluate the position of the signal's carrier after sampling

$$\begin{aligned} \pm\omega_{BB} &= \pm\omega_c - 2\pi \frac{n}{T_S} \\ &= \pm 2\pi \cdot 77.5 \cdot 10^3 - 2\pi \cdot 3 \cdot 24 \cdot 10^3 = \pm 2\pi \cdot 5.5 \cdot 10^3 \text{Hz} \end{aligned} \tag{3.10}$$

The signal located at the low intermediate frequency has to be converted to the baseband to be decoded. For such a purpose, when the signal varies relatively slowly, the Goertzel algorithm can be used. The demodulation can be provided just by finding the amplitude of the bin; such evaluation does not need any complex computation. The difference equation

$$|y(n+1)| = \sqrt{d^2(n+1) - 2\cos\left(2\pi \frac{k}{N}\right) d(n+1)d(n) + d^2(n)} \tag{3.11}$$

evaluates the absolute value from the state variables *d(n)*.

Due to the rectangular windowing the leakage of the side lobes is high. The example of using the Hanning window is also discussed in [17] together with a more detailed description of the DCF77 receiver and the prototype measurement results. The description of the implementation of the DCF77 receiver and the discussion of the implementation problems is published in [18].

3.1.2. Goertzel filter composition

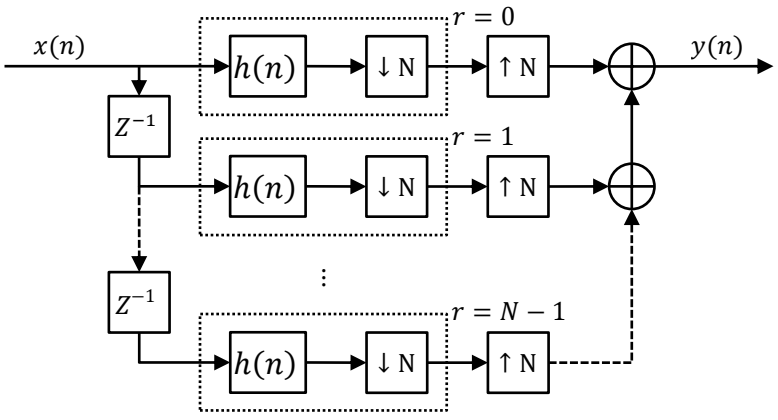

Figure 3.2: Goertzel filter composition.

Consider the digital system in Figure 3.2. The system consists of *N* mutually delayed branches of the Goertzel filter. The signals are then successively multiplexed to the output; this operation is depicted by upsampling and summing the signals.

The dashed rectangle wraps the Goertzel filter which is represented by its impulse response $h(n)$ and decimation ability with factor *N*. Each branch is indexed by the index *r*.

The output spectrum of the proposed system according to Figure 3.2 can be expressed by a relation

$$Y(\omega) = \sum_{r=0}^{N-1} \left(\frac{1}{N} \sum_{k=0}^{N-1} H\left(\omega - 2\pi \frac{k}{MT_S}\right) \cdot X\left(\omega - 2\pi \frac{k}{MT_S}\right) \right) \cdot e^{-j\omega r T_S}. \tag{3.12}$$

Finally, the output signal has been proved to be the input signal convoluted with the Goertzel impulse response

$$Y(\omega) = H(\omega) \cdot X(\omega) \xrightarrow{\mathcal{F}^{-1}-transform} y(n) = x(n) * h(n). \tag{3.13}$$

It has been found that the proposed system eliminates the decimation property of the Goertzel filter, thus, it may be used as a downconverter with a specified decimation factor independently on its filtration characteristics.

3.1.3. Goertzel filter modification for real frequency

From its nature the discrete Fourier transform evaluates the spectrum of the input signal that is sampled and each sample (bin) corresponds to a precisely defined frequency. It is not possible to simply change coefficients in the fast Fourier transform algorithms to change the frequency of the bin. The Goertzel algorithm is different; its coefficient can be very easily changed to tune the Goertzel filter to any arbitrary frequency from the range limited by the sampling frequency [19]. This is true, but it behaves differently when using a simple rectangular window.

The convolution is limited to N samples and k is the same variable as in the Fourier transform, but from now it is a real parameter ($k \in \mathbb{R}$). The relation between the tuned frequency and the variable k is expressed in

$$\frac{k}{N} = \frac{f_c}{f_S} \tag{3.14}$$

where f_S is the sampling frequency, f_c is the tuned frequency and N is the length of the Fourier transform. The exact analytical evaluation of the response of the Goertzel algorithm to real harmonic signal of the magnitude M and the phase φ on which it is tuned after some computation yields the relation

$$\begin{aligned} Y_k(n) &= \sum_{m=0}^{N-1} M \cdot \cos\left(2\pi \frac{k}{N} m + \varphi\right) e^{j2\pi \frac{k}{N}(n-m)} \\ &= \frac{M}{2}\left(N e^{-j\varphi} + e^{j\varphi} \frac{1 - e^{-j4\pi k}}{1 - e^{-j4\pi \frac{k}{N}}} \right). \end{aligned} \tag{3.15}$$

The first addend corresponds to one side spectral amplification of the Fourier transform and also the Goertzel algorithm. The second parameter is obviously zero whenever k is an integer ($k \in \mathbb{Z}$) and that is in agreement with the discrete Fourier transform. However, since k is real, it is nonzero and the resulting value is not equal to really applied signal parameters. The distortion comes from the opposite side of the Fourier spectrum as spectral leakage and can be eliminated by additional post-processing or pre-processing.

Substitution according to

$$A = \frac{1 - e^{-j4\pi k}}{1 - e^{-j4\pi \frac{k}{N}}} \tag{3.16}$$

and

$$B = Me^{-j\varphi} \tag{3.17}$$

yields

$$Y_k(n) = \frac{1}{2}(BN + B^*A) \tag{3.18}$$

which is a more convenient relation for the following operations.

Equation (3.18) can be solved for unknown B, where Y_k is the Goertzel filter output, so the result

$$B = \frac{2}{AA^* - N^2}(AY_k^* - NY_k) \tag{3.19}$$

is actually the compensation for the real k.

From now it is possible to find the compensation coefficients for an algebraic form of the result for a polar form. For clarity the real and imaginary parts of the values are denoted only by the indexes R and I, respectively, the index k is omitted. Equations (3.20) through (3.24) show the compensation coefficients for the real and imaginary parts.

$$B_R = Y_I Q_1 + Y_R(Q_2 - Q_3) \tag{3.20}$$

$$B_I = Y_R Q_1 - Y_I(Q_2 + Q_3) \tag{3.21}$$

$$Q_1 = \frac{2A_I}{A_R^2 + A_I^2 - N^2} \tag{3.22}$$

$$Q_2 = \frac{2A_R}{A_R^2 + A_I^2 - N^2} \tag{3.23}$$

$$Q_3 = \frac{2N}{A_R^2 + A_I^2 - N^2} \tag{3.24}$$

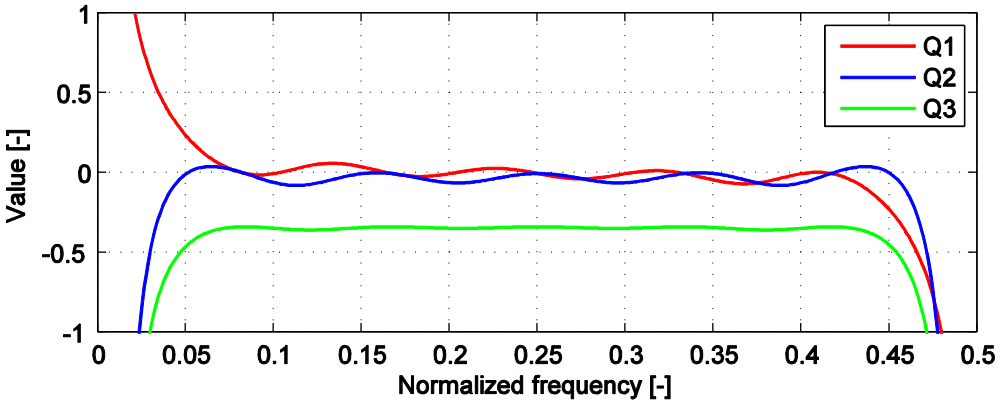

Figure 3.3: Compensation coefficients for algebraic form for $N = 6$.

Notice that when k is an integer, i.e. A is zero, the coefficients collapse to one weighting coefficient $\frac{2}{N}$. The character of the coefficients is clearly seen in Figure 3.3. Similarly the coefficients can be derived for the realization more convenient structure of the Goertzel algorithm and separate magnitude and phase calculation.

The influence of the compensation is presented on the real example. Firstly, the magnitude computation is visualized as waterfall spectrograms in Figure 3.4. Bad result is given by the uncompensated algorithm for the non-integer value of k as shown in spectrogram c). After compensation the distorting pattern is suppressed around the central frequency and the evolution of the central frequency magnitude is constantly unity as is in accordance to the input signal. The distorting pattern on the spectrograms causing undesired fluctuations of the output magnitude value is in fact the result of spectral leakage from negative to the positive frequency side and vice versa. The shorter the Goertzel filter and the closer the central frequency to the band edges is the more apparent the leakage is. The proposed compensation technique recalculates the magnitude to be more or less matching the real value and is effective but does not solve the problem from the root of the cause. To get better results, it is necessary to use another technique to suppress spectral leakage to a minimum, e.g. windowing.

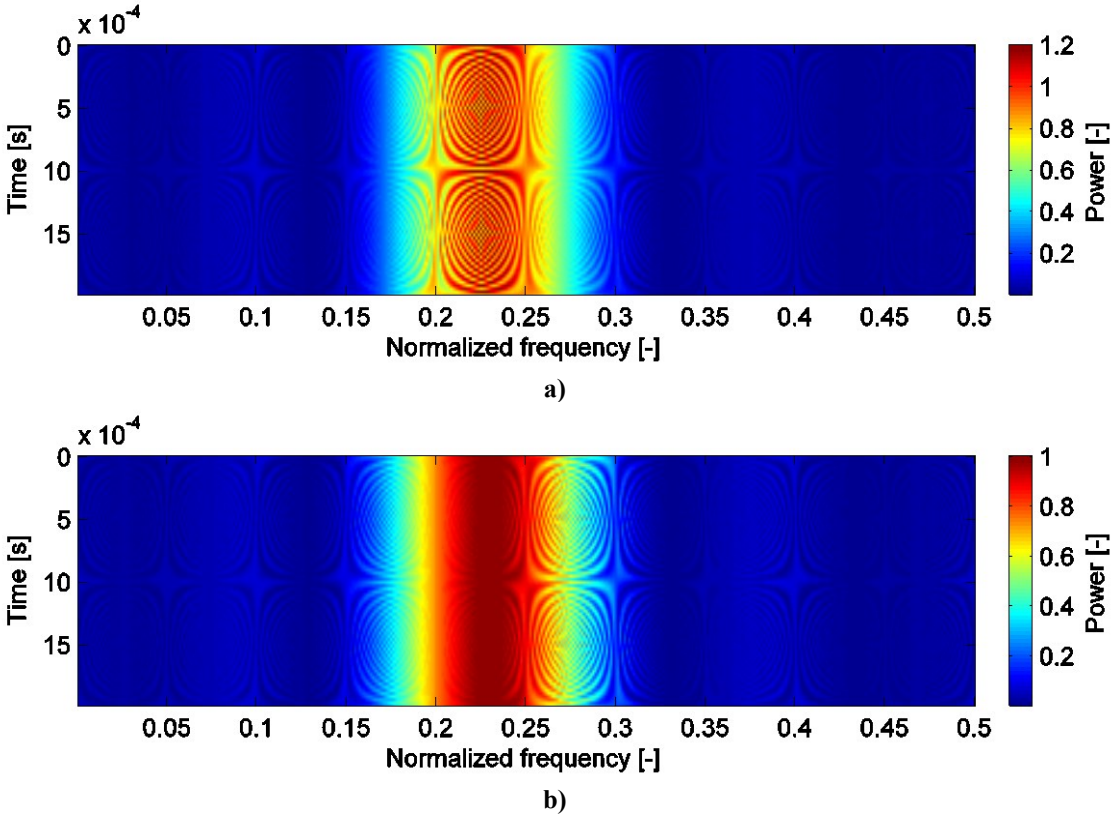

Figure 3.4: Spectrograms of the Goertzel filter for $N = 12$ –**a)** Uncompensated filter for $k = 2.3$, **b)** Compensated filter for $k = 2.3$.

3.1.4. Improved structure of the decimating filter

The filtration characteristic of the Goertzel algorithm has due to its simplicity a quite low level of signal suppression outside the pass band and the subsequent decimation causes aliasing noise. Common knowledge suggests weighting of the impulse response by one of special weighting windows the same way as is common for an FFT analysis. Such a way is, of

course, possible, but there is a question: Can we somehow modify the Goertzel algorithm to make its impulse response to be smoother? And, we can.

The impulse response of the original Goertzel algorithm is a complex harmonic signal and as we know the special combination of two harmonic signals of different but near frequencies results in beat tones. The idea is to use beat modulation to shape the impulse response. First, we take two impulse responses indexed as *A*

$$h_A(n) = e^{j2\pi\frac{k+d}{N}n} \tag{3.25}$$

and *B*

$$h_B(n) = e^{j2\pi\frac{k-d}{N}n} \tag{3.26}$$

respectively, which are moved from the center frequency by the offset *d*, and calculate the convolution. The impulse response of the Goertzel filter is cut by the rectangular window and the convoluted impulse characteristics also have to be limited. The convolution, finally, equals

$$h_{M1}(n) = \sum_{s=0}^{n} h_A(s)h_B(n-s) = e^{j2\pi\frac{k}{N}n}\frac{\sin\left(2\pi\frac{d}{N}(n+1)\right)}{\sin\left(2\pi\frac{d}{N}\right)}. \tag{3.27}$$

Now we have to find the value *d*, where one beat of the impulse response fits to the length of *N* samples, so it has minimal values on its edges. Assuming reasonable conditions we define

$$\begin{aligned} h_{M1}(N-1) &= e^{-j2\pi\frac{k}{N}} \\ e^{-j2\pi\frac{k}{N}} &= e^{-j2\pi\frac{k}{N}}\frac{\sin(2\pi d)}{\sin\left(2\pi\frac{d}{N}\right)} \\ \sin(2\pi d) &= \sin\left(2\pi\frac{d}{N}\right). \end{aligned} \tag{3.28}$$

The first suitable solution of (3.28) is

$$d = \frac{1}{2}\frac{N}{N+1} \tag{3.29}$$

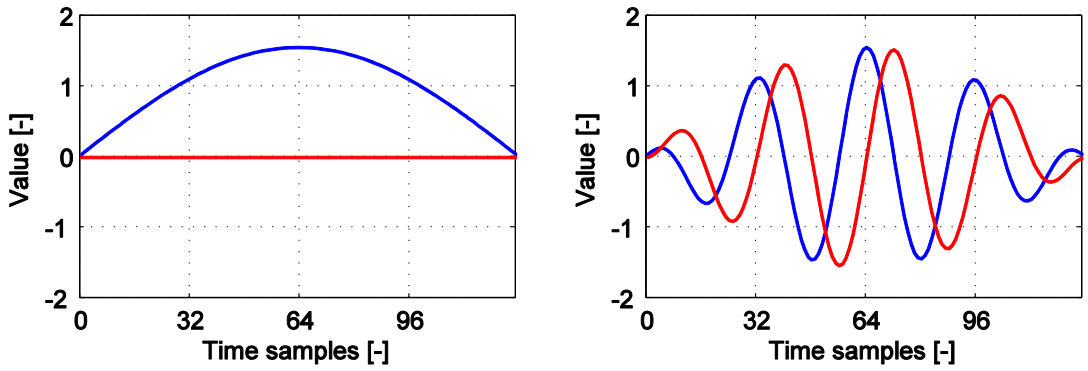

Figure 3.5: Impulse responses of the modified Goertzel filter for *N = 128* and *k = 0* (left), *k = 4* (right).

In Figure 3.5 are shown the examples of derived impulse responses for the baseband ($k = 0$) and the passband ($k = 4$). Both characteristics are normalized to its length N and are visualized as real (red) and imaginary (blue) parts.

The derivation of the frequency characteristics is similar to the Goertzel filter frequency characteristics derivation and after some manipulation yields

$$H_{M1}(n) = \frac{\left(1 - e^{-\alpha(N+1)} e^{\frac{\beta}{N}+\beta}\right)\left(e^{\frac{\beta}{N}} - e^{-\alpha}\right) - \left(1 - e^{-\alpha(N+1)} e^{-\left(\frac{\beta}{N}+\beta\right)}\right)\left(e^{-\frac{\beta}{N}} - e^{-\alpha}\right)}{\left(e^{\frac{\beta}{N}} - e^{-\frac{\beta}{N}}\right)\left(e^{-\frac{\beta}{N}} - e^{-\alpha}\right)\left(e^{\frac{\beta}{N}} - e^{-\alpha}\right)} \tag{3.30}$$

with the substitutions

$$e^{\alpha} = e^{j2\pi\left(f - \frac{k}{N}\right)} \tag{3.31}$$

and

$$e^{\beta} = e^{j2\pi d}. \tag{3.32}$$

The result is too complex, because it also includes non-optimal characteristics. If we assume the usage in the optimal configuration, we substitute the relation for the optimal value of d (3.29). The resulting simplification lies in

$$\beta = j\pi \frac{N}{N+1} \rightarrow e^{\frac{\beta}{N}+\beta} = -1. \tag{3.33}$$

Substituting (3.33) into (3.30) after some manipulation yields the final frequency characteristic for the optimal modified filter

$$H_{M1}(f) = \frac{\cos\left(\pi\left(f - \frac{k}{N}\right)(N+1)\right)}{\cos\left(2\pi\left(f - \frac{k}{N}\right)\right) - \cos\left(\frac{\pi}{N+1}\right)} e^{-j\pi\left(f - \frac{k}{N}\right)(N-1)}. \tag{3.34}$$

The normalization coefficient for the transfer function can be found by setting the transfer at the interested frequency to one, then the multiplicative coefficient is equal to the reciprocal value of

$$H_{M1}\left(\frac{k}{N}\right) = \frac{1}{1 - \cos\left(\frac{\pi}{N+1}\right)}. \tag{3.35}$$

Figure 3.6 and Figure 3.7 compare the frequency characteristics with the Goertzel filter characteristics. Obviously the suppression of a stop band is rapidly improved and even the bandwidth is not excessively widened compared to windowing by the Hann or Hamming windows [17].

In final form of the transfer function of the modified filter

$$H_{M1}(z) = \frac{1 - \tilde{C}_1 z^{-1} + \tilde{C}_2 z^{-2}}{1 - C_2(z^{-1} + z^{-3}) + C_1 z^{-2} + z^{-4}} \tag{3.36}$$

the coefficients are reformulated to a more convenient form

$$\tilde{C}_1 = 2\cos\left(2\pi\frac{d}{N}\right)e^{-j2\pi\frac{k}{N}}, \tag{3.37}$$

$$\tilde{C}_2 = e^{-j4\pi\frac{k}{N}}, \tag{3.38}$$

$$C_1 = 2\left(\cos\left(4\pi\frac{k}{N}\right) + \cos\left(4\pi\frac{d}{N}\right) + 1\right), \tag{3.39}$$

$$C_2 = 4\cos\left(2\pi\frac{k}{N}\right)\cos\left(2\pi\frac{d}{N}\right). \tag{3.40}$$

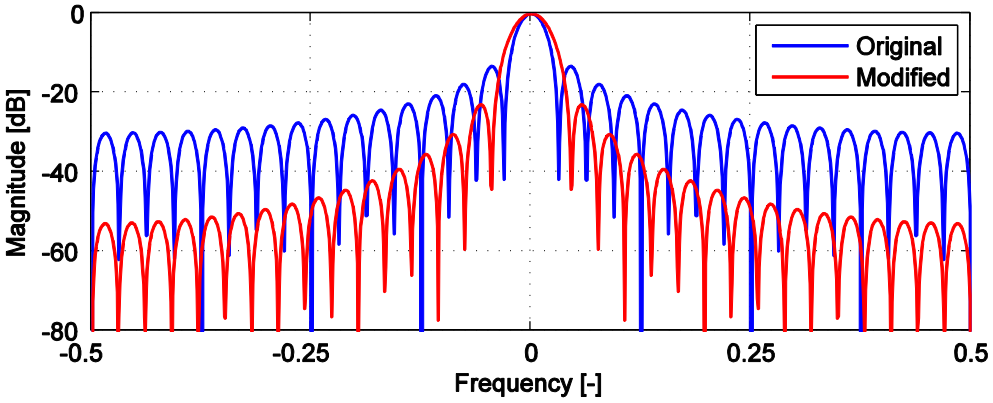

Figure 3.6: Magnitude frequency characteristics of the Goertzel filter and its modified version for $N = 32$ and $k = 0$.

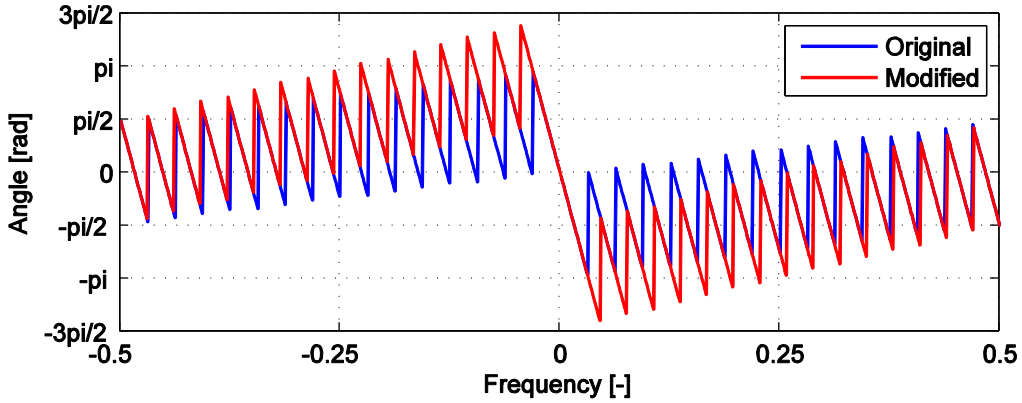

Figure 3.7: Phase frequency characteristics of the Goertzel filter and its modified version for $N = 32$ and $k = 0$.

The transfer function (3.36) is realized by the difference equation

$$\begin{aligned} y(n) &= x(n) - \tilde{C}_3 x(n-1) + \tilde{C}_2 x(n-2) \\ &\quad + C_2\big(y(n-1) + y(n-3)\big) - C_1 y(n-2) - y(n-4). \end{aligned} \tag{3.41}$$

The realization structure in Figure 3.8 is the application of the modified Goertzel filter as a downconverter according to the previous discussion. It was expected that the derived structure will be twice more complex than the original Goertzel downconverter, but the C_2 coefficient can be applied after summation, which saves one multiplication in the recursive part. The resulting number of multiplication in the recursive part is then 2 and equals the

number of multiplication in the structure using the original Goertzel algorithm applied to the window weighted signal.

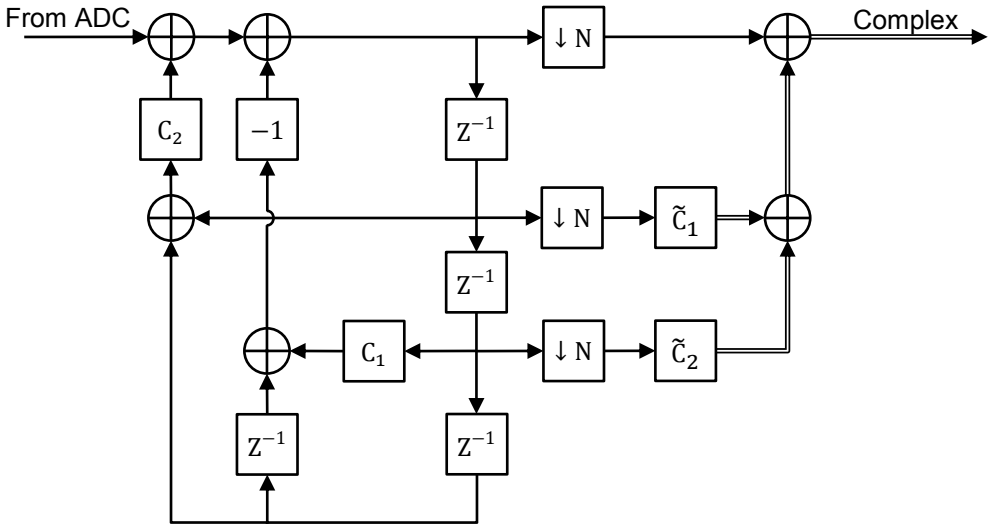

Figure 3.8: Signal diagram of the modified Goertzel filter.

3.2. Digital downconverter performance

3.2.1. BER influence

The frequency characteristics of the CIC-filter and the Goertzel filter are the same, so its comparison is not relevant; we perform a comparison between the Goertzel filter and its modified version in the first step. Secondly, the filters are compared with a half decimation factor, where the half sampling frequency reduction, but significantly lower aliasing are expected. In Figure 3.9 there are depicted two aliasing situations for the Goertzel filter ($N = 8$, $k = 0$). It is obvious, that the side lobes contribute to aliasing noise several fold less in the case of the half decimation factor (right plot). The characteristic of the pass band is flatter and aliasing is lower near the center frequency. The Goertzel algorithm characteristic has zeros periodically located in such a way that they, after decimation, fit right to the center of the desired band and they have an essential impact on aliasing noise performance. The modified algorithm has different positions of zeros as is seen in Figure 3.6 and aliasing performance should be expected significantly worse even if it, from a global view, looks better.

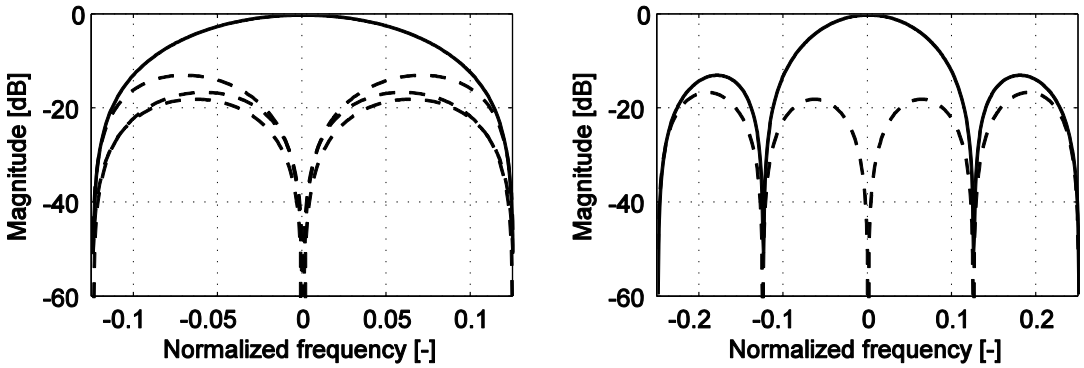

Figure 3.9: Downconverter filter aliasing with decimation factor M (left) and $\frac{M}{2}$ (right).

According to the analysis, we based our calculations on Parseval's theorem. The integration over the pass band is

$$S(f_S, N, r) = \frac{1}{N^2 \cdot f_S} \int_{-\frac{r \cdot f_S}{2}}^{\frac{r \cdot f_S}{2}} |H(f)|^2 df \tag{3.42}$$

and analyzed parameters are the desired bandwidth (bandwidth ratio) r and the filter length N, which in this case equals the decimation factor. The aliasing noise has to be expressed differently

$$N_G(f_S, N, r) = \frac{1}{N^2 \cdot f_S} \sum_{k=0}^{N-1} \int_{-\frac{r \cdot f_S}{2}}^{\frac{r \cdot f_S}{2}} |H_G(f, k, N)|^2 df. \tag{3.43}$$

The integration is calculated over the same bandwidth of all discrete frequencies ($k \in \mathbb{Z}$).

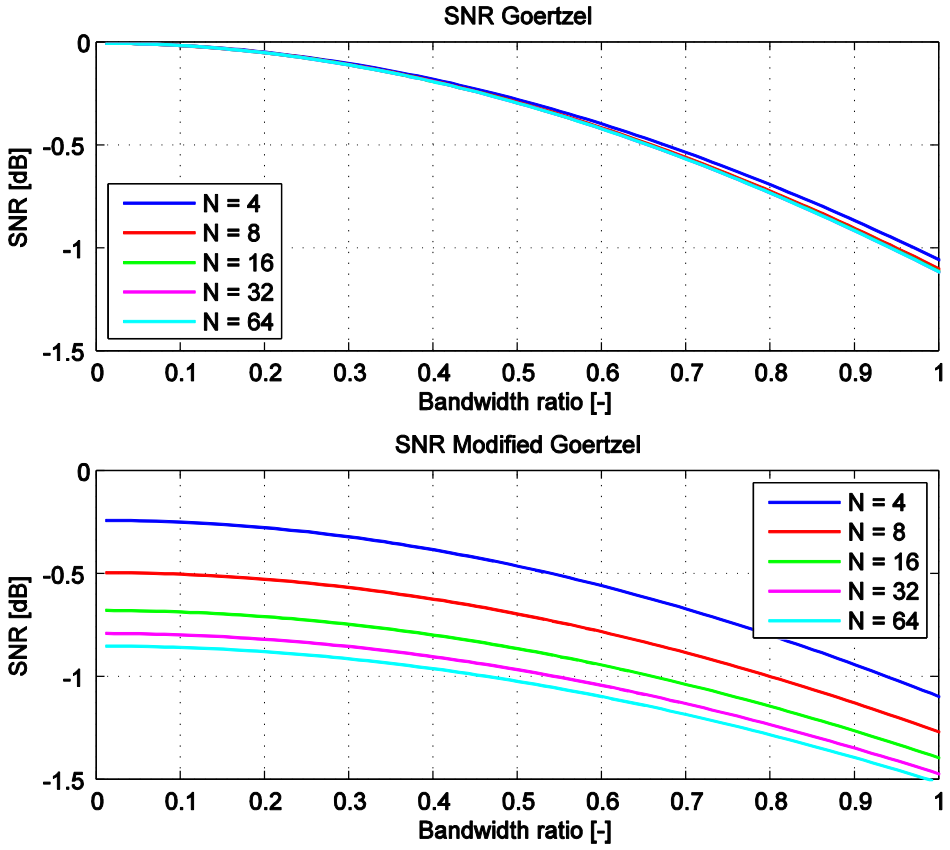

Figure 3.10: Aliasing noise performance of the Goertzel and modified Goertzel downconverter.

The results for the Goertzel downconverter and the modified Goertzel filter downconverter are depicted in Figure 3.10.

The results say that the bandwidth ratio significantly influences BER degradation and is the lowest for narrowband signals. The Goertzel length does not influence the results significantly. If we look at the modified Goertzel downconverter, the results are completely different. The pass lobe of the filter is wider and worsens BER performance due to its main contribution to aliasing noise power. The different location of zeros of the magnitude characteristic causes the aliasing noise to spread and the bandwidth ratio then does not have a

very helpful impact. The differences for each length N are also caused by the different zero locations.

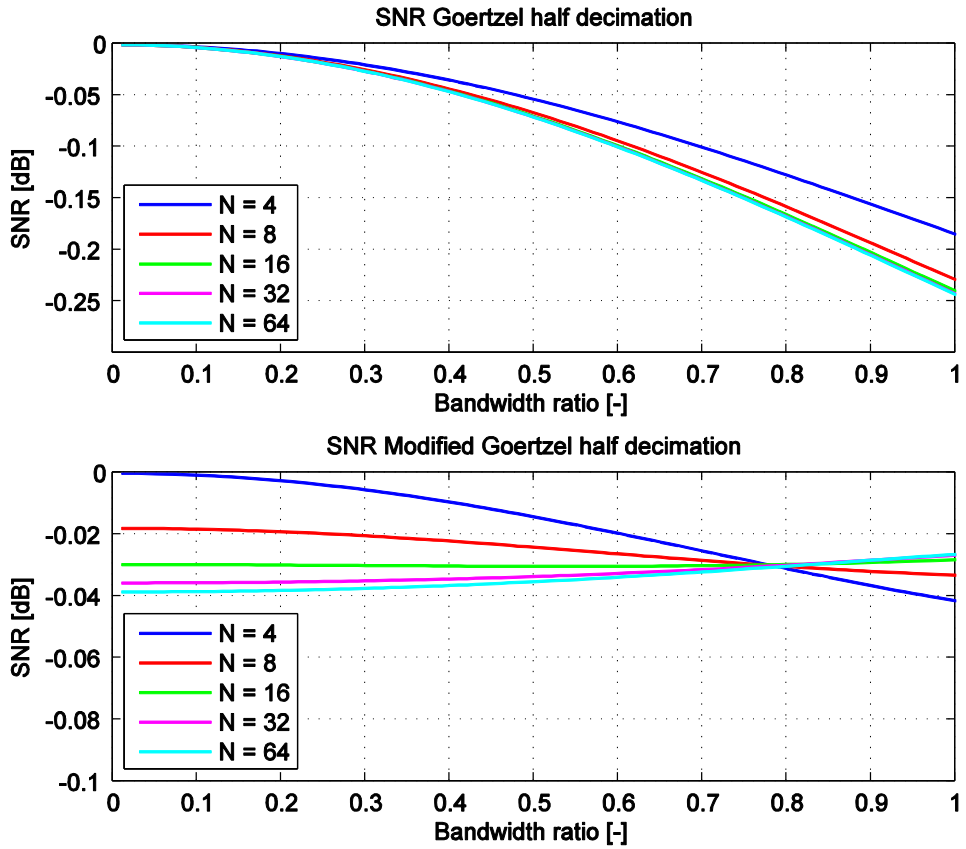

Figure 3.11: Aliasing noise performance of the Goertzel and modified Goertzel downconverter for the half decimation factor.

The noise contribution of the half decimation factor versions comes newly from every second integer frequency

$$N_G(f_S, N, r) = \frac{1}{N^2 \cdot f_S} \sum_{k=0}^{\frac{N}{2}-1} \int_{-\frac{r \cdot f_S}{2}}^{\frac{r \cdot f_S}{2}} |H_G(f, 2k, N)|^2 df. \tag{3.44}$$

The results are shown in Figure 3.11. The situation is different for the modified filter, the influence of the main lobe has been removed and better suppression of the side lobes is obvious. BER degradation stays very low over the whole bandwidth ratio interval and significantly surpasses the Goertzel downconverter for higher bandwidths.

3.2.2. Computational demands

Once the target platform, where the downconverter is planned to be implemented, the computational demands of each algorithm have to be known. One of the assessment methods is the evaluation of multiplication and addition operation demands. The actual demands can then easily be judged over lots of platforms including microcontrollers and gate arrays.

The results summarized in Table 3.1 show that the original Goertzel algorithm is more effective from the number of operation point of view. The Goertzel algorithm is able to

reduce sampling rate, which is important especially in sequential systems like microcontrollers. The downfall of the improved algorithms is their complexity, but the benefit is better characteristics.

Table 3.1: Downconverter computational demands.

Downconverter type	Multiplications	Additions	Memory space
CIC	*2M + 2*	*2M + 2*	*5*
Goertzel	*N + 2*	*2N + 1*	*5*
Modified Goertzel	*2N + 4*	*4N + 3*	*10*
Goertzel – half decimation	*2N + 4*	*4N + 2*	*N/2 + 10*
Modified Goertzel – half decimation	*4N + 8*	*8N + 6*	*N/2 + 20*

3.2.3. Quantization errors of the algorithms

The general issues of overflowing and rounding errors are strongly dependent on the final implementation, but we can find general influence of the coefficient quantization error. The function of the Goertzel filter has two poles from which one is eliminated by a zero. The error of C coefficient ε causes misalignment of the poles

$$1 - 2(C + \varepsilon)z^{-1} + z^{-2} = \left(1 - e^{j\cos^{-1}(C+\varepsilon)}\right)\left(1 - e^{j\cos^{-1}(C+\varepsilon)}\right), \tag{3.45}$$

but its movement is limited to the unity circuit for relatively small errors, which do not make the coefficient be out of the range $\langle 1; -1\rangle$. It means that the quantization error causes frequency tuning error.

The coefficient of the poles C is common to be implemented as a signed fractional number and the real position of the pole is expressed by

$$e^{-j\cos^{-1}(C+\varepsilon)} = \cos(cos^{-1}(C + \varepsilon)) - j\sin(cos^{-1}(C + \varepsilon)). \tag{3.46}$$

If the complex coefficient of the zero $\tilde{C}$ is implemented separately for the real and imaginary parts, the complex quantization error will affect the zero position according to

$$\tilde{C} = e^{-j2\pi\frac{k}{N}} + \tilde{\varepsilon} = (\cos(\alpha) + Re\{\tilde{\varepsilon}\}) - j(\sin(\alpha) + Im\{\tilde{\varepsilon}\}). \tag{3.47}$$

The real part of the complex coefficient $\tilde{C}$ is identical to the real coefficient C, and therefore we can assume that the implementation of these coefficients are also identical or even the real part of the $\tilde{C}$ coefficient is used instead of the C coefficient with improved memory savings. This assumption implies that the error ε equals the error $Re\{\tilde{\varepsilon}\}$. Now the misalignment of the pole and its compensation zero is

$$\vec{e} = j\left(\sin(\alpha) + Im\{\tilde{\varepsilon}\} - \sqrt{1 - (Re\{\tilde{\varepsilon}\} + \cos(\alpha))^2}\right). \tag{3.48}$$

The error vector says that the mentioned way of implementation minimizes the zero from the pole misalignment only to the imaginary dimension. The function has its extremes at the edges of the sampled frequency band.

From the analysis of the frequency tuning error caused by the quantization error of the coefficient C we can find the relation

$$e_f = \frac{\cos^{-1}\left(\cos\left(2\pi\frac{k}{N}\right)+\varepsilon\right)}{2\pi}. \tag{3.49}$$

It is obvious that the most critical region is also near the edges of the sampled frequency band. A possible way to deal with this issue is pre-filtering as published in [20].

3.3. Simulink tests

The tests of the proposed downconverters were achieved by simulations in MATLAB Simulink. Each testing model has more or less been composed from the available design blocks. An assessing criterion was the sensitivity of the RF system to SNR performance. The chain of the general tested model is depicted in Figure 3.12. A random signal modulated onto the RF carrier was put through a radio channel and then processed by the tested item, i.e. the demodulator block. The "received" data was compared to the original copy and the Bit Error Rate was estimated.

Figure 3.12: General schematic of the tested model.

3.3.1. BERtool models

BERtool is a simple MATLAB tool for bit error rate simulation of communication systems. It is possible to plot and export simulation results as the bit error ratio dependent on the signal energy to signal power ratio. The reference BEP function for BPSK modulation is

$$BEP = Q\left(\sqrt{2\cdot 10^{\frac{E_b/N_0}{10}}}\right) = \frac{1}{2}erfc\left(\sqrt{10^{\frac{E_b}{N_0\cdot 10}}}\right) \tag{3.50}$$

where the $Q(x)$ function is a probability function of the Gaussian probability distribution and $erfc(x)$ is a complementary Gaussian error function.

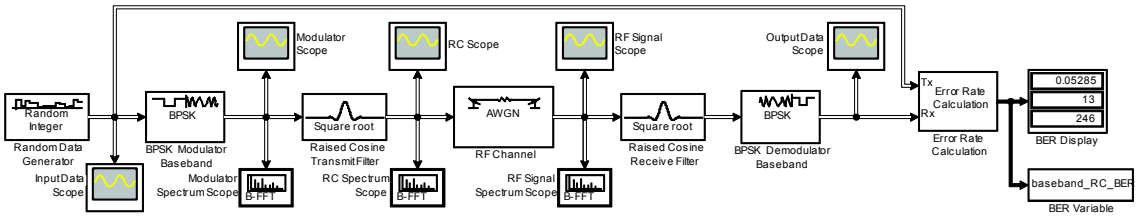

Figure 3.13: BERtool model of baseband BPSK modulator with Square-Root Raised Cosine filter.

The influence of the Raised-cosine filter was also tested; the model is depicted in Figure 3.13. The implemented filter is the square-root type, therefore two filters are used, one on the

transmitter side and one on the receiver side. In Figure 3.14 there is depicted the model for the Goertzel algorithm based downconverter simulations.

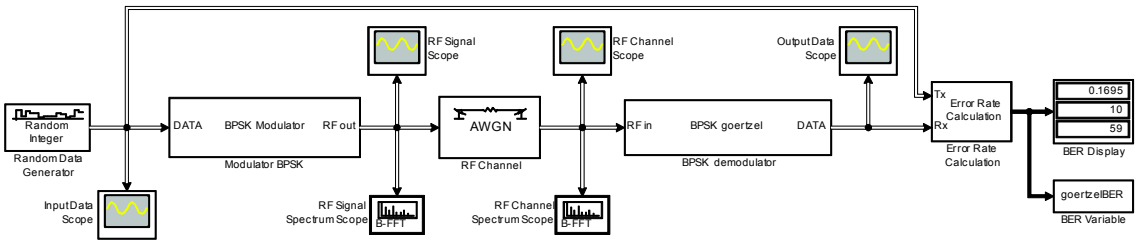

Figure 3.14: BERtool model of Goertzel downconverter.

The models for the modified Goertzel downconverter and for the version of half decimation factor were not tested by BERtool, but a special script to see the difference from the original Goertzel downconverter immediately. Since the half decimation factor version gives twice more samples than the symbol rate, the downconverter must be followed by an additional decimator consisting of a half-band filter and a downsampling module.

3.3.2. BER simulation results

The BER characteristics of the proposed downconversion algorithms obtained by simulation are shown in the following figures. In Figure 3.15 there are shown characteristics for the proposed Goertzel and modified Goertzel downconverters in two versions dependent on the used main lobe width. The results may be surprising because they are in strong disagreement with the theoretical assumption in chapter 3.2.1. However, the explanation is clear. In the theoretical analysis we supposed the out-of-band signals to be noise with a destructive effect on the in-band signal, but the unfiltered BPSK signal has a significant part of its power out of the downconverted band. The full-band Goertzel downconverter has the filtration characteristic somehow "matched" to this power spectral density, because it comprises the rectangular window of the same width as the input signal symbol period, and therefore aliasing is partly constructive. The modified version of the Goertzel downconverter has better attenuation in the stop-band and has zeros located differently which effectively suppresses the out-of-band partly constructive components and consequently worsens the overall BER characteristic. Additionally, since the signal power is spread, after filtration the E_b/N_0 ratio is worse than expected. The same effect works for the half-band versions with the difference that the Goertzel downconverter filtration characteristic is no longer matched to the input signal.

The simulation results are obviously different in Figure 3.16, where the Raised-Cosine filter is used on the transmission side and the output power is corrected to the nominal power. In these cases the modified Goertzel downconverter performs better. We suppose that the roll-off factor of values around 0.5 is more desirable than 1.0, because there is sufficient attenuation of the side lobes, and in this case the downconverters perform in expected order. The modified Goertzel half-band downconverter gave us the best results while both full-band downconverters are the worst. The characteristic of the baseband transmission is shown for comparison and checking the power level. The performance of the downconverters with the filter with a roll-off factor of 1.0 is again influenced by constructive spectral leakage caused by weak attenuation of the closest side lobes.

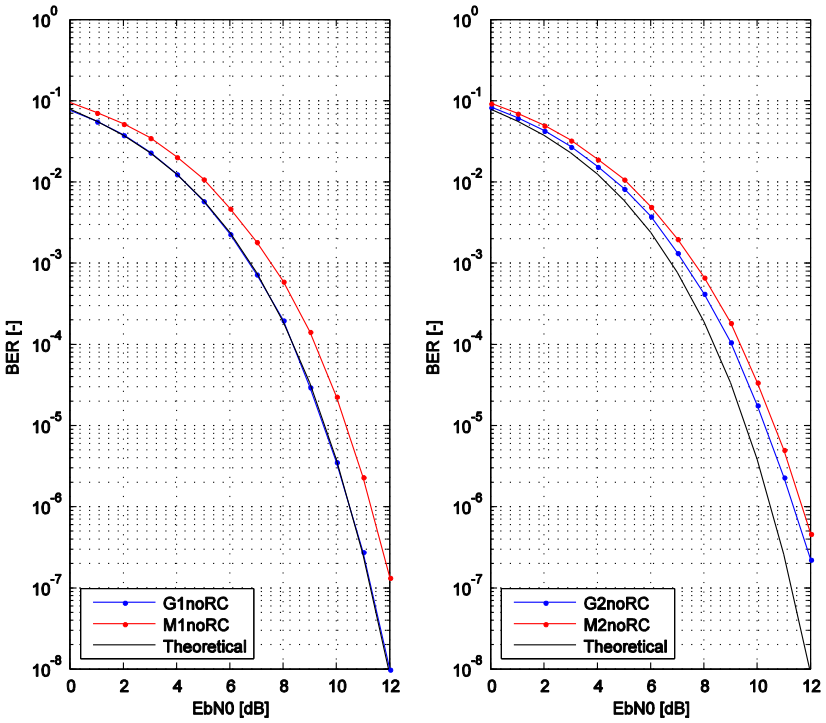

Figure 3.15: BER simulation results of the Goertzel and modified Goertzel downconverters with no matched filter on the transmission side. The full-band version on the left hand side and the half-band version on the right hand side.

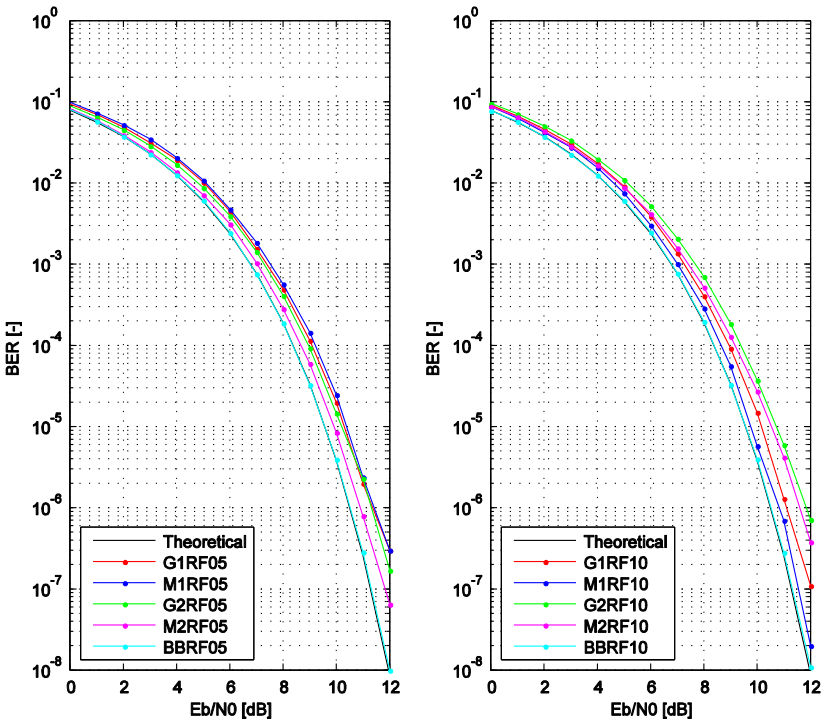

Figure 3.16: BER simulation results of the Goertzel and modified Goertzel downconverters and both full-band and half-band versions with the Raised-Cosine matched filter at the transmission side. The simulation for the filter with the roll-off factor 0.5 on the left hand side and for the roll-off factor 1.0 on the right hand side.

4. Carrier synchronization

The correct demodulation of received radio frequency signals lies in the knowledge of carrier parameters. Static systems with a non-critical working environment are satisfied with a non-coherent demodulation. In the case of listening to far objects, typically satellites and the deep-space probes, which are often moving so fast, that the Doppler frequency shift becomes significant degrading aspect, using coherent and partially coherent demodulation giving a margin in the detection error performance is inevitable. Such digital systems need special algorithms for carrier parameter estimation.

4.1. Frequency estimation

4.1.1. Spectrum averaging frequency estimator

The specific spectral characteristics of the receiving signals may allow us to find another approach to carrier frequency estimation. The complete BPSK signal with the modulation index β of carrier frequency ω_c and phase φ_c is defined by

$$s_{BPSK}(t) = \sqrt{2P}\cos(\beta)\sin(\omega_c t + \varphi_c) + \sqrt{2P}\sin(\beta)\sum_{k=-\infty}^{\infty} c_k p(t - kT_R)\cos(\omega_c t + \varphi_c). \tag{4.1}$$

The P stands for RMS signal power, which is, by the modulation index, divided into carrier power and data symbol c_k power. The symbols are modeled by the pulse function $p(t)$, where T_R is the symbol period. The index R is used to prevent it being mixed up with the sampling period T_S.

The baseband BPSK signal spectrum with assumption of the zero carrier frequency and the zero carrier phase equals

$$S_{SCBB}(\omega) = \frac{\sin\left(\omega\frac{T_R}{2}\right)}{\omega\frac{T_R}{2}}. \tag{4.2}$$

The spectrum of the BPSK signal is symmetric and this is the key property of the proposed algorithm, firstly because we suppose that the symmetry of the spectrum is unnatural, and secondly it uses the whole signal power for detection, which is important for detection in the noisy environment.

In Figure 4.1, there is shown the block diagram of the proposed algorithm.

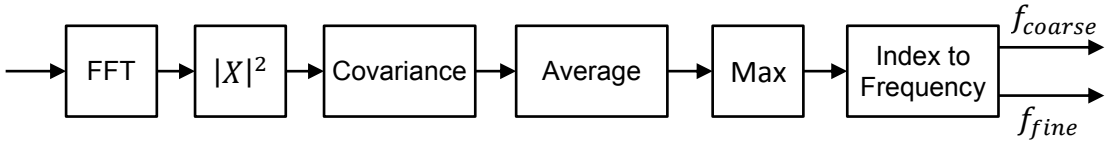

Figure 4.1: Spectrum averaging frequency estimator.

The spectrum is estimated by the fast Fourier transform (FFT). Since the transform is applied to the finite length generally non-deterministic signal, the estimation more or less differs from reality. It is usual to use windowing technique to improve the estimation parameters; the spectral resolution and the spectral leakage are two key contradictory parameters of the windows. In our case the high dynamic range of the signal is also important,

because of the focus on the signals with a high level of additional noise, and every window more or less significantly decreases the dynamic of the analyzed signal. A rectangular window has very high spectral leakage, but excellent resolution characteristic for the signals of comparable strength and signal power is not weighted. That is why the rectangular window is a good choice for the spectral analysis within the frequency estimator, at least in the first step of the development.

The result of FFT applied to the real signal has a symmetric magnitude to which the correlation can be applied. The correlation function will result in a high peak if the signals are similar to each other. As proposed in [21], the correlation does not converge for signals with a non-zero mean, so a better way is to use the auto-covariance function, where the mean is estimated and subtracted first. The algorithm then has the following steps; the power spectrum estimation

$$P(k) = |S(k)|^2 = Re\{S(k)\}^2 + Im\{S(k)\}^2, \tag{4.3}$$

mean estimation

$$\bar{P} = \frac{1}{N}\sum_{n=0}^{N-1} P(n) \tag{4.4}$$

and covariance function estimation using the auto-correlation of the AC component

$$P_{AC}(k) = P(k) - \bar{P} \tag{4.5}$$

$$C(k) = \sum_{n=-\infty}^{\infty} P_{AC}(n)P_{AC}(n+k). \tag{4.6}$$

The sum with limits of the correlation corrected to *N* samples is

$$C(k) = \sum_{n=0}^{N-k} P_{AC}(n)P_{AC}(n+k). \tag{4.7}$$

Signal containing strong noise can be easily averaged. The averaging algorithm used is a simple exponential cumulation for the frames of *2N* samples. The averaged covariance peaks for the two noise level examples are shown in Figure 4.2.

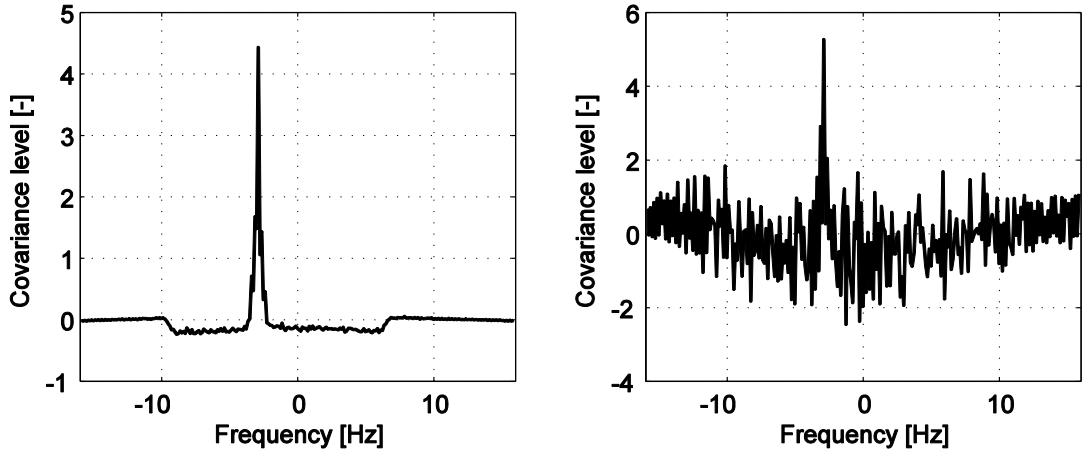

Figure 4.2 Averaged covariance function for $\frac{E_b}{N_0} = 10dB$ (left) and $\frac{E_b}{N0} = 0dB$ (right).

The position of the peak defines the carrier frequency of the BPSK signal. The desired frequency f_{cc} from the peak position index k_c is then calculated using the formula

$$f_{cc} = f_S \frac{N - k_c - 1}{2N}. \tag{4.8}$$

N defines the length of FFT, and because spectrum estimation is discretized in frequency, the resulting frequency estimation suffers from quantization error $\Delta f = \frac{f_S}{N}$. The result is then considered as coarse estimate. The carrier frequency lying between the FFT bins can be exactly evaluated from the characteristic of the rectangular window, but the calculation and resulting formula is expected to be too complex, and therefore an empirical approximation formula was found for $\bar{C}(k_l) > \bar{C}(k_r)$

$$f_c = f_{cc} + \frac{\Delta f}{2}\left(1 - \frac{\bar{C}(k_r)}{\bar{C}(k_l)}\right) \tag{4.9}$$

and for $\bar{C}(k_l) < \bar{C}(k_r)$

$$f_c = f_{cc} - \frac{\Delta f}{2}\left(1 - \frac{\bar{C}(k_l)}{\bar{C}(k_r)}\right) \tag{4.10}$$

where $\bar{C}$ is the averaged covariance output and *l* and *r* indexes the left hand neighbor sample from the coarse estimation and the right hand sample respectively.

4.1.2. Closed loop spectrum averaging frequency estimator

The spectral averaging frequency estimator proposed in the previous chapter gives the absolute frequency of the BPSK signal. The frequency can be used as the error signal of the closed loop estimator too. The input signal is slowly moved to the baseband and then the frequency estimator gives zero frequency, which is correct. The only complication is the averaging algorithm within the estimator, since the input signal is moving in the frequency domain, the averaged spectrum will be disrupted. The solution for such an issue is to make the loop slow enough to allow the estimator to efficiently track the spectral changes.

4.1.3. Modified closed loop spectrum averaging frequency estimator

The modified estimator block diagram is shown in Figure 4.3. The frequency error is provided by additional linear operations. The covariance peak is differentiated to linearly transform the maximum to the zero crossing.

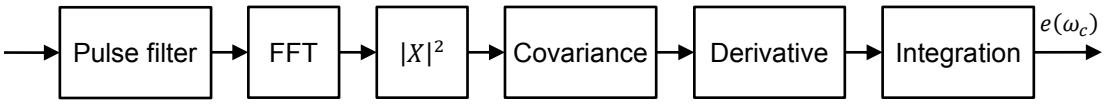

Figure 4.3 Modified spectrum averaging frequency estimator.

Figure 4.4 shows a single instance of the covariance peak and its derivative. Even though the noise level is low, the derivative is very noisy. However, the shape of the derivative is antisymmetric around the zero frequency and thus the integral over the frequency interval is on average zero. To eliminate the parasitic ripple at the curve's edges, the integration range is narrowed. Then the locking range of the closed loop estimator will be widened. Every deviation from the nominal carrier frequency will result in the positive or negative error deviation and the loop will force to compensate the error.

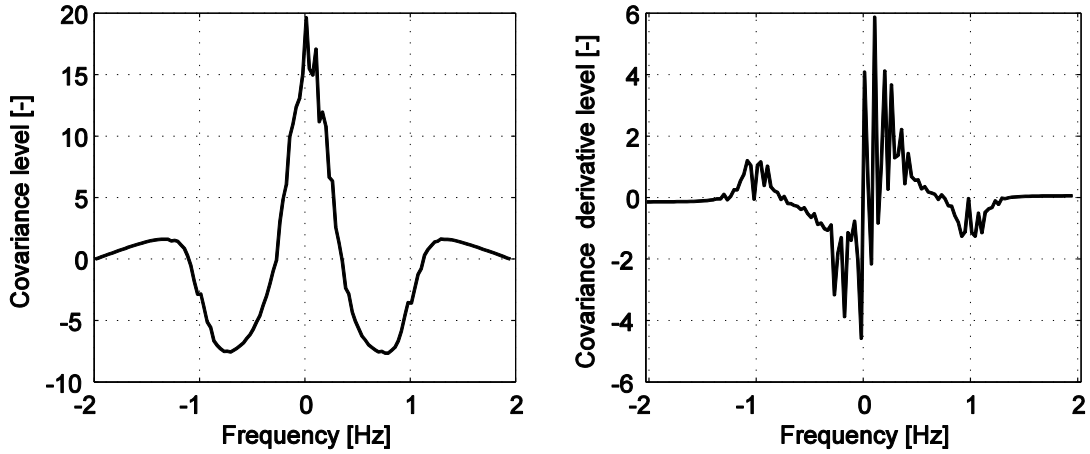

Figure 4.4 Covariance peak of the modified spectrum averaging algorithm (left) and its derivative (right).

At the very beginning of the block schematic in Figure 4.3, there is a pulse filter, which is typical also for the ML estimator and plays several roles. At first, the filter acts as a matched filter, which is necessary especially for filters like root RC filters. It is a low pass filter, which suppresses noise at higher frequencies and significantly improves the SNR of the signal. On the other hand, the low pass filter narrows the range of loop acquisition and if the signal is not pre-downconverted correctly, the loop will not be able to lock anymore. The pulse filter is also very important for covariance peak shaping. The filter is set to downsample the input signal to fit the FFT resolution to the desired bandwidth and it noticeably widens the covariance pulse. The peak width has an essential impact on the shape of the S-curve.

4.2. Simulink tests

Carrier synchronization systems are usually characterized by an error estimator transfer function, the so called S-curve, and a frequency estimate variance dependent on the signal noise performance. The chain of the general simulation model of the frequency estimators is shown in Figure 4.5.

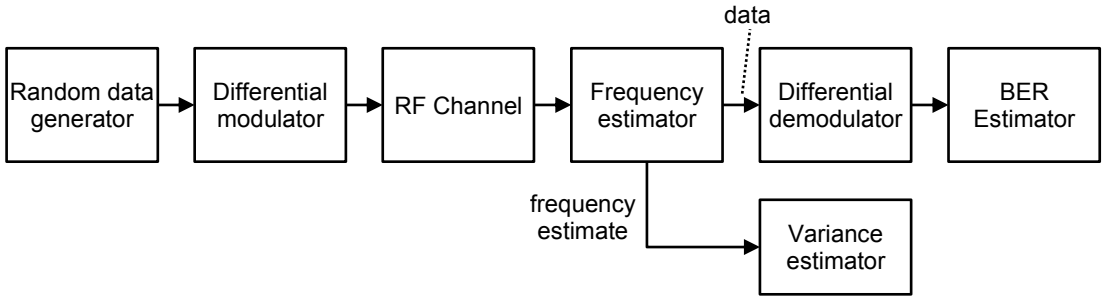

Figure 4.5 General schematic of the frequency estimator simulation model.

4.2.1. Spectrum averaging frequency estimator model

The model of the open loop spectrum averaging frequency estimator is shown in Figure 4.6. It starts with the buffer followed by the m-file function of which its code is depicted in Listing 4.1. The size of the buffer indirectly sets the size of the FFT window, which can be seen in the code, where the size is extracted. As is expected from the function block name, the code estimates the covariance function of the signal spectrum. The covariance function bearing the carrier frequency in the form of the conspicuous peak is averaged by the

exponential cumulation with a period of $2N-1$ samples. The last m-file function block contains the code providing the peak position seeking and recalculation of the position into the frequency estimate. The peak position seeking is based on the maximum position index searching and the discrete frequency calculated form (4.8) is then refined with inclusion of the maximum value and values of the nearest neighbor samples according to equations (4.9) and (4.10).

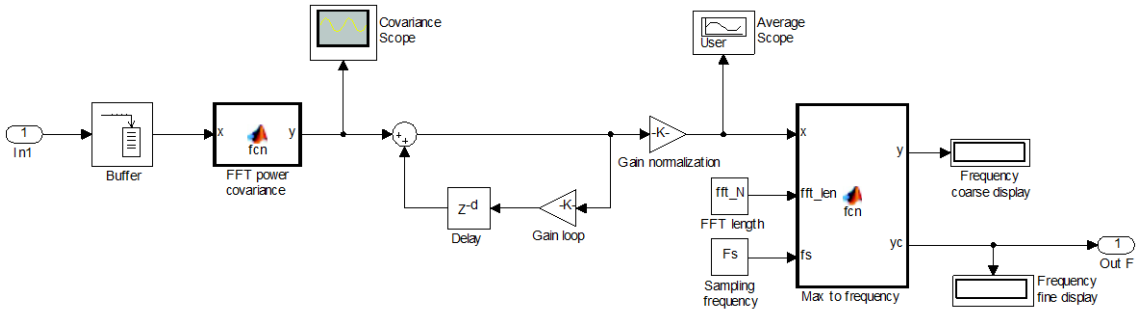

Figure 4.6 Open loop spectrum averaging frequency estimator.

```
function y = fcn(x)

len = length(x);
y = zeros(2*len - 1, 1);

x = (abs(fftshift(fft(x)))/(len/2)).^2;

x = x - sum(x)/length(x);
xA = x;
xB = [zeros(len - 1, 1); flipud(x); zeros(len - 1, 1)];

for i = 1:(2*len - 1)
    y(i) = 0;
    for j = 1:len
        y(i) = y(i) + xA(j)*xB(j + i - 1);
    end
end
```

Listing 4.1 FFT power covariance code.

The Simulink model of the frequency estimator using the open loop spectrum averaging frequency estimator is shown in Figure 4.7.

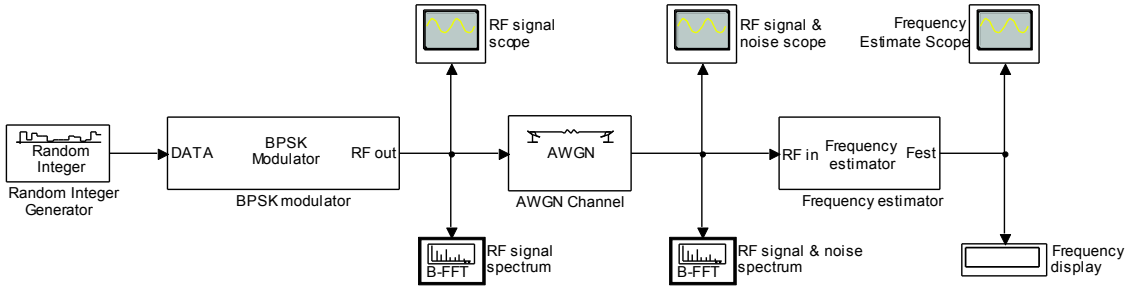

Figure 4.7 Open loop spectrum averaging frequency estimator model.

The closed loop spectrum averaging frequency estimator model is based only on its modified version according to Figure 4.3. The pulse filter is in our case the square root filter. The decimation factor of the pulse filter is in this model adjustable in dependence on the desired error estimator bandwidth and the noise immunity.

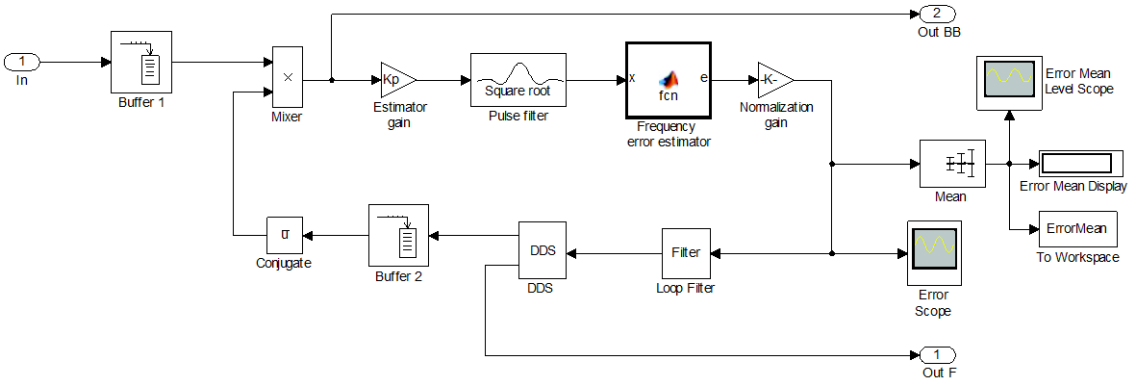

Figure 4.8 Closed loop spectrum averaging frequency estimator.

The code of the error estimator is based on the code of the open loop estimator, but with several modifications. Since the decimation factor of the pulse filter is adjustable, due to the covariance peak shaping, the spectrum of the oversampled signal will contain spectral components at irrelevant frequencies. These components are put away from the covariance calculation. The covariance estimate is then differentiated to convert the value to the error function. Finally, the function is filtered by the integration, realized by the sum over specified interval centered on the zero frequency. The testing model for the closed loop spectrum averaging frequency estimator is in Figure 4.9.

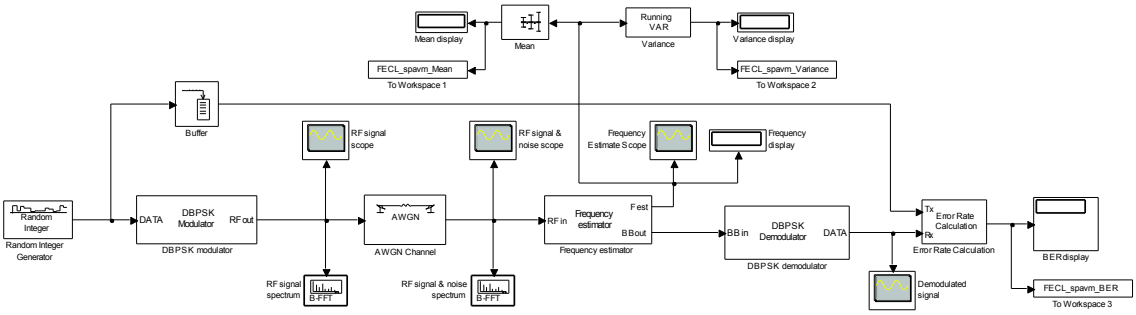

Figure 4.9 Closed loop spectrum averaging frequency estimator model.

4.2.2. Estimation simulation results

In Figure 4.10 there are shown the simulated S-curves of the ML closed loop and spectrum averaging closed loop frequency estimators. The function is the immediate reaction of the error estimator to the carrier frequency variations. It is possible to read out the range of acquisition if the carrier frequency is out of the S-curve; the error estimator provides no reaction to such an offset and thus the system is not able to synchronize. The slope of the linear region crossing the zero level in the middle of the S-curve defines the tracking performance of the system. Comparing the ML and spectrum averaging estimator S-curves shows that the systems have nearly identical acquisition and tracking characteristics with the difference that the spectrum averaging system has a slightly narrower acquisition region.

Unlike the BPSK signal, the theoretical BER of DBPSK modulation is slightly different. The difference lies in the fact that the single detection error for differentially coded modulation results in two, not necessarily consecutive, data bits. The bit error probability for the differentially coherent DBPSK is [23]

$$BEP = \frac{1}{2}\exp\left(-\frac{E_b}{N_0}\right). \tag{4.11}$$

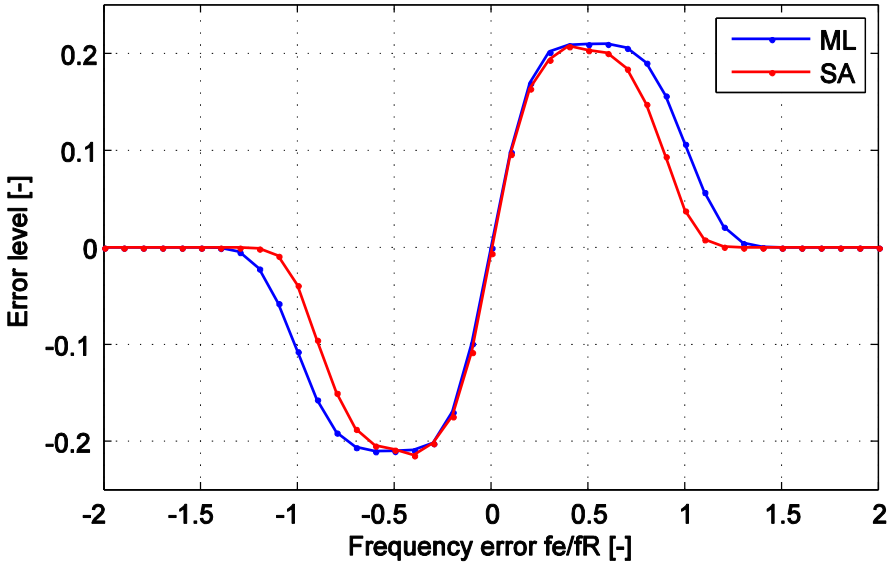

Figure 4.10 Frequency estimators S-curves.

The bit error rates measured by the simulation of the frequency estimator models are plotted in Figure 4.11 (left). It is nicely seen that the simulated BER of both models are in good conformity with the theoretical error probability BEP and it indicates that both estimators work fine and do not have a big impact on detection.

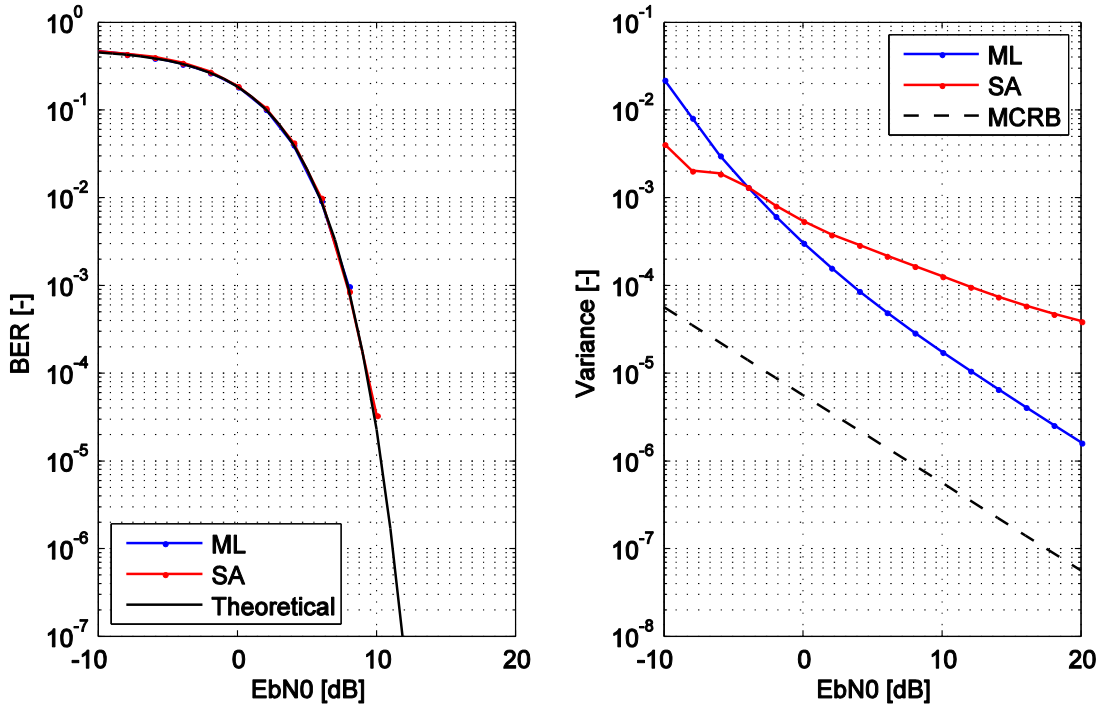

Figure 4.11 Frequency estimators BER results (left) and carrier variance (right).

The right plot of Figure 4.11 shows the variance performance of the models compared to the modified Cramer-Rao bound. Both estimators are quite far from ideal performance. There are many averaged parameters, and therefore our expectation could not be more optimistic. The spectrum averaging frequency estimator was designed for carrier synchronization of signals in very noisy environments within none-aided systems (without

data aid or symbol timing). Comparing to the maximum likelihood estimator, the evolution is different, for higher E_b/N_0 ratios the ML estimator has undoubtedly better performance. For higher noise power, however, the performance of the introduced novel estimator comes closer and even crosses the ML line, where it shows better performance. Of course, we have to be critical and state that the region of better performance is very close to the useless signal to noise ratios in usual systems. On the other hand, the algorithm seemingly has potential for further interests.

5. Experimental tests

The methods discussed previously are intended for signal processing within the reception of the narrowband satellite signals. We obtained a record of a wideband signal from a fixed frequency SDR system, which includes the desired narrowband BPSK modulated signal from a PSAT satellite distorted by the Doppler shift during flyover. The PSK31 transponder carried by the PSAT satellite was designed at the department of Radioelectronics in collaboration with United States Naval Academy and the satellite was launched on May 20, 2015.

5.1. Frequency synchronization

The recorded signal was loaded from a *.wav file to the MATLAB workspace as a timeseries. Firstly, the signal is pre-processed to limit its bandwidth to the range of the possible Doppler shift with its center frequency near to the satellite transmission frequency. All used frequency estimators are not able to synchronize the phase that is needed for coherent demodulation, but are used as a necessary frequency aid since the Costas loop, acting as the phase synchronizer, has a very limited acquisition range. The frequency aid from the open loop estimator is led to the Costas loop directly by addition to the DDS tuning signal. This is an efficient solution because the frequency conversion is performed by a single mixer within the Costas loop. The situation is different for the closed loop frequency estimators where the loop requires its own mixer, and therefore the frequency correction is prepended to the Costas loop and the system requires two independent mixers in each loop.

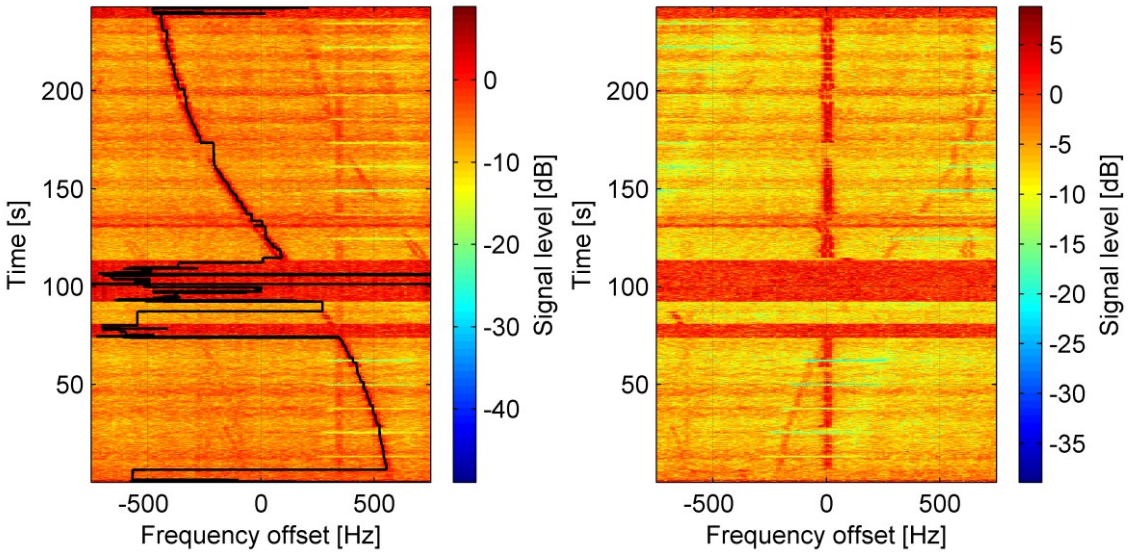

Figure 5.1: Waterfall spectrogram with the frequency estimate from the open loop spectrum averaging estimator – coarse estimate (left), corrected signal (right).

The transmitted signal is the PSK31, which is used for very slow communication of keyboard typing speed, from this radio-teletype (RTTY) [25]. The carrier signal is modulated by BPSK modulation by differentially coded data of speed 31.25 Bd. The useful bandwidth of the PSK31 signal is therefore about 60 Hz. In contrast, the Doppler shift at carrier frequency 435 MHz from the PSAT satellite at low Earth orbit (LEO) reaches ±600 Hz.

In Figure 5.1, there are shown the waterfall spectrograms of the recorded sample signal of the sampled bandwidth 1500 Hz. This signal was led unfiltered to the open loop spectrum averaging frequency estimator to obtain the frequency estimate. The estimator does not need any setting of an initial frequency, it uses all the input bandwidth. The results show that the coarse estimation is very successful. In the signal, there are noisy parts with a lack of the PSK31 signal, but the recovery is fairly fast.

On the contrary, the closed loop frequency estimators employ lowpass filtration at its input and this significantly narrows the acquisition range. Initial frequency setting is therefore important for correct acquisition. The simulation results for the closed loop spectrum averaging and closed loop maximum likelihood frequency estimators are shown in Figure 5.2. The initial frequency was set to 450 Hz, which can be supposed as near to the expected frequency offset at the beginning of the satellite flyover.

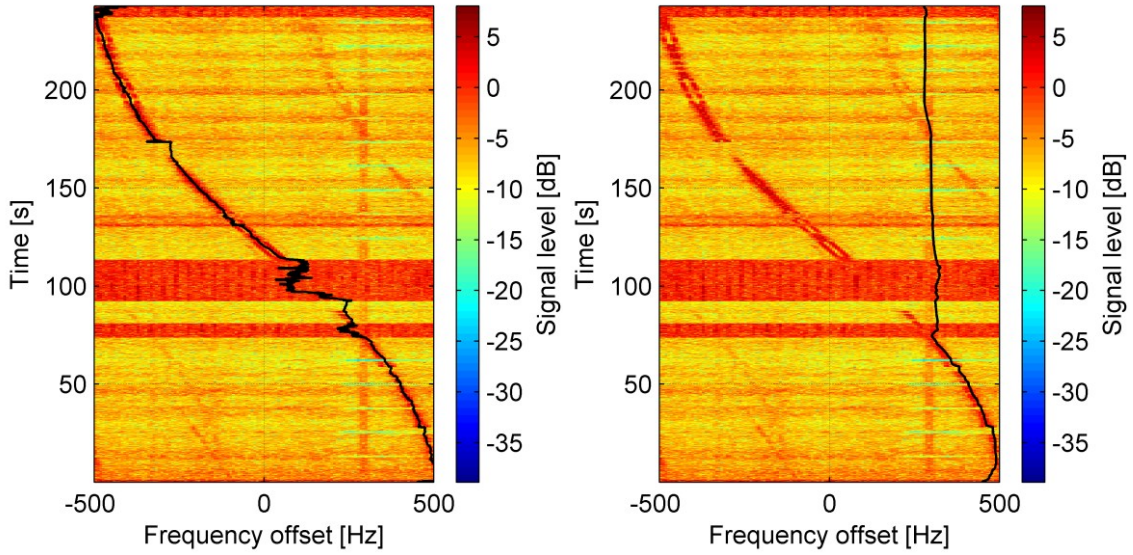

Figure 5.2: Waterfall spectrogram with the frequency estimate from the closed loop estimators with 450 Hz initial frequency – spectrum averaging (left), maximum likelihood (right).

It is obvious that unlike the CL SA estimator, the CL ML estimator has lost lock even after a short period of signal loss and therefore using CL ML is disqualified for frequency synchronization of such signals in this straightforward version. However, the results show that with a properly set initial frequency, the CL SA estimator is applicable for the signals with strong Doppler shifts and limited drop-out times.

The benefits of the OL SA frequency estimator now seem to be undisputable, but there is an additional point. The curves of fine estimations of each method show different residual noise and this naturally affects the detection error rate. The experiments showed the main drawback of the spectrum averaging methods – high estimation noise. Comparing the closed loop estimators, the Costas loop locking times are significantly faster in the case of the ML estimator.

5.2. Digital downconversion

Signal recording also includes a signal from the ground radio-beacon. The signal is also PSK31 modulated with no frequency Doppler shift. The signal bandwidth to the sampled bandwidth ratio is around 100 and it is an ideal opportunity for applying the Goertzel downconverter. The beacon signal center frequency is about 320 Hz in the 12 kHz sampled record. The decimation factor of all the developed downconverters is set to 32, thus, the resulting signal has a sampling frequency of 375 Hz and the signal of interest is aliased to the center frequency of -55 Hz.

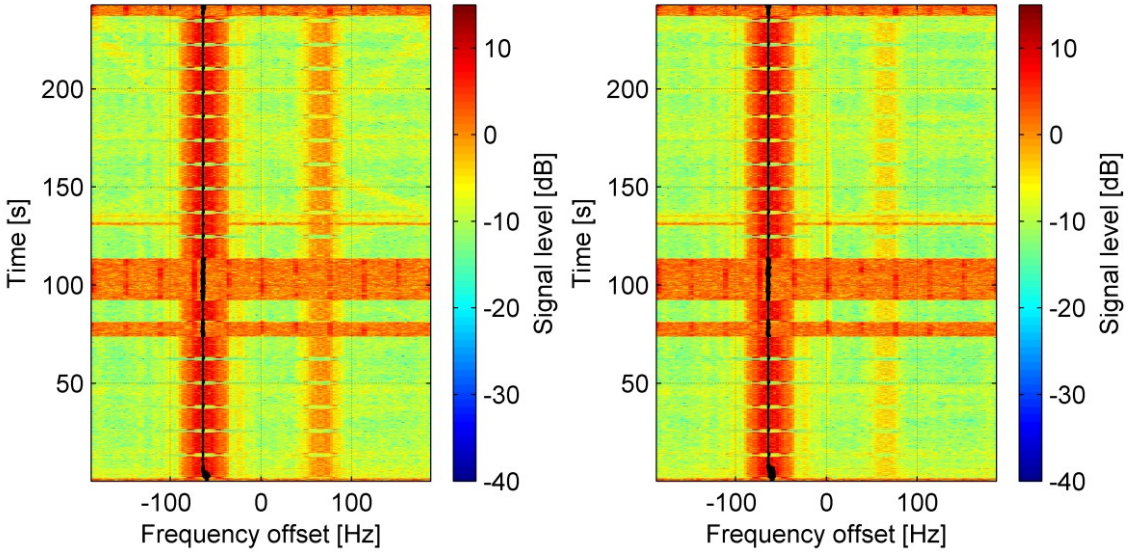

Figure 5.3: Waterfall signal spectrogram after downconversion by the Goertzel full-band downconverter (left) and by the Goertzel modified full-band downconverter (right).

Figure 5.3 shows the spectrograms of the full-band Goertzel downconverter and its modified version with the Costas loop frequency estimate (black line). There is also visible a weaker signal at a complementary frequency, this is actually the -320 Hz signal complement of the real beacon signal. The beacon signal is at relatively low frequency within the sampled band, and therefore the two complements are very close and thus hard to be filtered out.

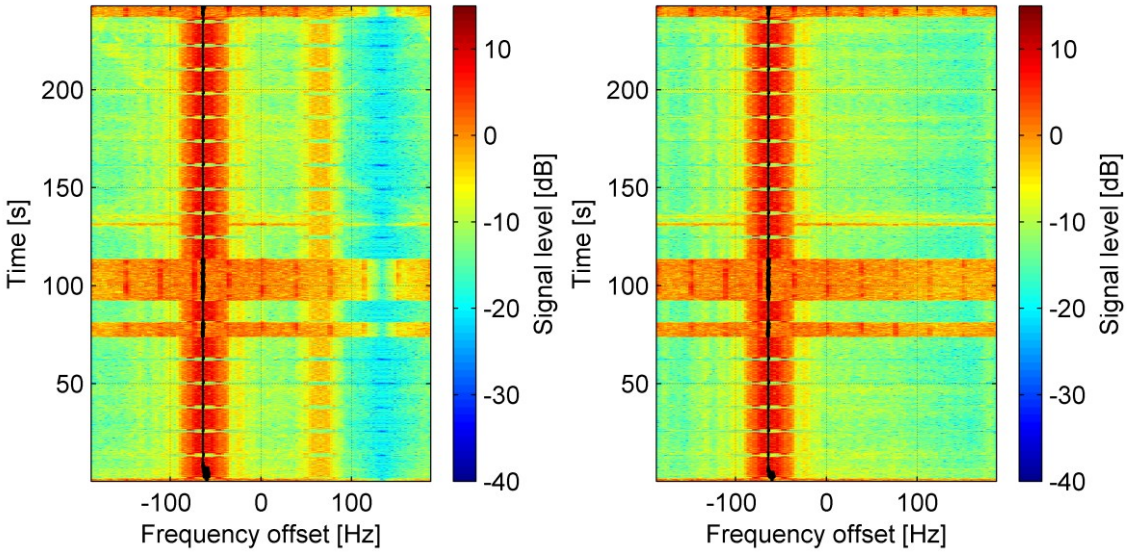

Figure 5.4: Waterfall signal spectrogram after downconversion by the Goertzel half-band downconverter (left) and by the Goertzel modified half-band downconverter (right).

The following figures show the characteristics of each downconverter. The modified Goertzel downconverter has sharper attenuation of undesired bands and this is confirmed by a significantly lower level of an interfering component in Figure 5.3 right. The same situation can be observed in Figure 5.4 depicting the results of the half-band (HB) versions of the downconverter. The Goertzel HB downconverter performs strong attenuation at the edges of the sampled region caused by the well-defined zeros at its transfer function. Unlike the modified Goertzel HB version, the interfering component stays recognizable. The modified version has strong attenuation of the side bands, however, it should be remembered that the zeros are not defined well for aliasing minimization.

6. Conclusion

The dissertation is focused on the development of new digital signal processing algorithms for software defined receivers of narrowband satellite signals. Particularly, the thesis firstly deals with effective downconversion including filtration and downsampling and secondly with carrier frequency estimation of signals distorted by a strong Doppler shift and AWGN. These are the two main objectives of the thesis and the third one comprises the modeling of the developed algorithms and experimental tests.

The first part of the thesis is an introduction to downconversion and frequency estimation algorithms described in literature and used in practice. There are also laid the foundations such as sampling theory and used spectral effective modulations for space communications.

Digital downconversion is discussed in section 3. The novel approach is based on the Goertzel algorithm, which is a special form of the discrete Fourier transform calculation. Downconversion is provided by undersampling and bandpass filtration. This approach is typically avoided, but the Goertzel algorithm offers operations to be performed very effectively. It has been shown that the filtration characteristic is comparable to the CIC filter, which is often used in FPGA-based systems. The Goertzel algorithm allows effective signal power estimation that is useful for AM detection and it was proved by the DCF77 receiver application. The drawback of undersampling based downconversion is the discrete conversion frequency suggesting the algorithm to be employed in multirate downconverters. It is possible to tune the filtration characteristic to the real frequency, but the power calculation is affected by strong fluctuations in this case. This issue was solved by special coefficients included in the calculation. The calculation is performed on the low-rate side that keeps the algorithm's efficiency high. The bandwidth of the bandpass filter and the decimation factor are inseparable characteristics. It was found that the special constellation of Goertzel filters allows to set the decimation factor independently on the filter bandwidth. The constellation of two parallel Goertzel filters was employed as the half-decimation Goertzel downconverters and helped to suppress aliasing during downsampling. The impulse response of the downconverter was improved by doubling the zero and pole of the original Goertzel filter. Consequently, the side-band attenuation of the frequency response was significantly increased. From these discoveries, four different downconverters were derived – the full-decimation Goertzel downconverter, the half-decimation Goertzel downconverter employing the parallelization of two Goertzel downconverters, the full-decimation and half-decimation modified Goertzel downconverters employing the improved version of the Goertzel downconverter. The algorithms were theoretically analyzed from the points of view of BER performance, computational demands, and quantization errors. The algorithms were modeled in MATLAB Simulink and the theoretical results were confronted with simulation results

over the AWGN channel. Finally, the downconverters were subjected to tests with a real signal. All the results showed that the algorithms can be considered as useful for downconversion of narrowband signals within appropriate platforms as the first stage of multirate downconversion.

In section 4, we focused on carrier frequency estimation of BPSK modulated input signals. Firstly, the known theoretical foundations such as Cramer-Rao bounds and maximum likelihood approach to carrier parameter estimation were laid. The main contribution to the objective of establishing new frequency estimators for narrowband signals with strong Doppler shifts and a high level of AWGN is based on the cumulation of the covariance function of the signal spectrum magnitude and from this we call the algorithms "spectrum averaging". Both open and closed loop versions of the spectrum averaging frequency estimators were introduced. The closed loop estimator was, at first, based on the open loop estimator put into the control loop, but strong nonlinearity in the form of maximum search function made adjustability hard and the overall performance of the estimator was poor compared to the ML estimator. This, finally, disqualified this approach. In the second version of the closed loop estimator, the maximum search function was replaced by a set of linear functions and it allowed averaging to be performed by the loop filter. This resulted in an estimator with parameters more comparable to the ML version. For simulations and tests on the real signal, the algorithms were modeled in the MATLAB Simulink and also for decoding the models of the Costas loop and the codes of offline decoders were prepared. The new SA open loop and SA closed loop estimators and the reference ML closed loop estimators were tested on a real satellite signal with a strong Doppler shift. Both ML open and closed loop estimators employ a pulse filter that removes as much noise as possible. The estimate is then fine, but the narrow pulse filter also narrows the acquisition range. The acquisition range is the field in which the SA estimators can compete and even beat the ML ones. The price paid is then higher levels of estimation noise.

At this point, all the objectives of the thesis can be considered as accomplished. However, the novel algorithms presented in the thesis will be studied deeply in real-time applications. There could be many unknown issues connected with the implementation of the algorithms and its transformation to fixed-point architecture.

7. Selected references

[1] HAMKINS, J., SIMON, M. K. *Autonomous software-defined radio receivers for deep space applications* [online]. Hoboken, N.J.: Wiley-Interscience, 2006, xxii, 435 pages. [cit. 2013-04-29]. ISBN 978-047-0082-126. Available at: http://descanso.jpl.nasa.gov/Monograph/series9/Descanso9_Full_rev.pdf

[2] ZAPLATA, F., KASAL, M. Architektury a základní vzorkovací techniky SDR. *Elektrorevue* [online]. 2012, No. 43 [cit. 2013-04-14]. ISSN 1213-1539. Available at: http://www.elektrorevue.cz/cz/download/architektury-a-zakladni-vzorkovaci-techniky-sdr

[3] SIMON, M. K. *Bandwidth-Efficient Digital Modulation with Application to Deep-Space Communications* [online]. Jet Propulsion Laboratory, California Institute of Technology, 2001, 237 pages. [cit. 2013-04-12]. Available at: http://descanso.jpl.nasa.gov/Monograph/series3/complete1.pdf

[4] *Space engineering: Radio frequency and modulation*. The Netherlands: ESA Requirements and Standards Division, 2009, 81 pages. Available at: http://www.ecss.nl/forums/ecss/dispatch.cgi/standards/showFile/100742/d20090309095455/No/ECSS-E-ST-50-05C_Rev.1%286March2009%29.pdf

[5] BURNS, P. *Software defined radio for 3G*. Boston: Artech House, 2003, xix, 279 pages. ISBN 15-805-3347-7.

[6] KENINGTON, P. B. *RF and baseband techniques for software defined radio*. Boston: Artech House, 2005, xiii, 332 pages. Artech House mobile communications series. ISBN 1-58053-793-6.

[7] ARSLAN, H., (ed.). *Cognitive radio, software defined radio, and adaptive wireless systems*. Online-Ausg. Dordrecht: Springer, 2007. ISBN 978-140-2055-423.

[8] KHAN, S. A. *Digital design of signal processing systems: A practical approach*. Hoboken: John Wiley, 2011. ISBN 978-047-0974-698.

[9] ZAPLATA, F. *Algoritmy zpracování signálu na platformě AVR32*. Brno, 2011, 65 pages, Diploma thesis. FEEC, Brno University of Technology.

[10] LYONS, R. G. *Streamlining digital signal processing: A tricks of the trade guidebook*. Hoboken, N.J.: Wiley-Interscience, 2007, xiv, 322 pages. ISBN 978-047-0131-572.

[11] MEYR, H., MOENECLAEY, M. *Digital Communication Receivers: Synchronization, Channel Estimation, and Signal Processing*. vol. 2. Hoboken, NJ: Wiley-Interscience, 1997, 827 pages. ISBN 04-712-0057-3.

[12] XIONG, F. *Digital modulation techniques*. 2nd ed. Boston, MA: Artech House, 2006, xxi, 1017 pages. Artech House telecommunications library. ISBN 1-58053-863-0.

[13] MENGALI, U., D'ANDREA, A. N. *Synchronization techniques for digital receivers*. New York: Plenum Press, 1997, xiii, 520 pages. ISBN 03-064-5725-3.

[14] KAY, S. M. *Fundamentals of statistical signal processing: estimation theory*. Upper Saddle River, N.J.: Prentice Hall PTR, 1993, xii, 595 pages. Prentice Hall signal processing series. ISBN 01-334-5711-7.

[15] GARDNER, F. M. *Phaselock techniques*. 3rd ed. Hoboken, NJ: John Wiley, 2005, xxii, 425 pages. ISBN 04-714-3063-3.

[16] OPPENHEIM, A. V., SCHAFER, R. W., BUCK, J. R. *Discrete-time signal processing*. 2nd ed. Upper Saddle River, N.J.: Prentice Hall, 1999, xxvi, 870 pages. ISBN 01-375-4920-2.

[17] ZAPLATA, F., KASAL, M. Software defined DCF77 receiver. *Radioengineering,* 2013, No. 4, p. 1211-1217. ISSN: 1210- 2512.

[18] ZAPLATA, F., KASAL, M. SDR implementation for DCF77. *23rd International Conference Radioelektronika*. IEEE, 2013, p. 340-345. DOI: 10.1109/RadioElek.2013.6530943. ISBN 978-1-4673-5519-3.

[19] DE JESUS, M. A., TEIXEIRA, M., VICENTE, L., RODRIGUEZ, Y. Nonuniform Discrete short-time Fourier transform a Goertzel filter bank versus a FIR filtering approach. *49th IEEE International Midwest Symposium on Circuits and Systems*. IEEE, 2006, p. 188-192. DOI: 10.1109/MWSCAS.2006.382241. ISBN 1-4244-0172-0. ISSN 1548-3746.

[20] ZAPLATA, F., KASAL, M. Efficient Spectral Power Estimation on an Arbitrary Frequency Scale. *Radioengineering*. 2015, vol. 24: p. 178-184. DOI: 10.13164/re.2015.0178. ISSN 1210-2512.

[21] JAN, J. *Medical image processing, reconstruction, and restoration: Concepts and methods*. Boca Raton: Dekker/CRC Press, 2005, xxiii, 730 pages. Signal processing and communications, 24. ISBN 08-247-5849-8.

[22] RICE, M. *Digital communications: a discrete-time approach*. Upper Saddle River, N.J.: Pearson/Prentice Hall, 2009, xxii, 778 pages. ISBN 978-013-0304-971.

[23] SIMON M. K., ALOUINI K. M.-S. *Digital communication over fading channels: A unified approach to performance analysis*. New York: John Wiley, 2000. ISBN 04-712-0069-7.

[24] SKLAR, B. *Digital communications: fundamentals and applications*. 2nd ed. Upper Saddle River, N.J.: Prentice-Hall PTR, 2001, xxiv, 1079 pages. ISBN 01-308-4788-7.

[25] MARTINEZ, P. PSK31: A new radio-teletype mode. *ARRL* [online]. 1999, p. 3-9. [cit. 2015-06-04] Available at: http://www.arrl.org/files/file/Technology/tis/info/pdf/x9907003.pdf

Curriculum Vitae

Name: Filip ZÁPLATA

Born: March 28th 1987 in Chrudim

Contact: f.zaplata@gmail.com

Education

2011 – 15 **Brno University of Technology / Department of Radio Electronics**
Ph.D. study of Electronics and Communication
Dissertation on Advanced algorithms for satellite communication signal processing

2009 – 11 **Brno University of Technology / Department of Radio Electronics**
Master's study of Electronics and Communication
Diploma thesis on Signal Processing Algorithms on AVR32 Platform

2006 – 09 **Brno University of Technology / Department of Radio Electronics**
Bachelor's study of Electronics and Communication
Bachelor's thesis on Digital filtration with 8-bit processors

Experience

9/11 – 11/12 **VESLA s.r.o. Pardubice**
R&D engineer developing embedded software for signal processing and control in commercial DVB systems

Languages

English, Russian

Abstract

The dissertation is focused on software defined receivers intended for narrowband satellite communication. The satellite communication channel including deep space communication suffers from a high level of noise, typically modeled by AWGN, and from a strong Doppler shift of a signal caused by the unprecedented speed of an object in motion. The dissertation shows possible approaches to the issues of computationally efficient digital downconversion of narrowband signals and the carrier frequency estimation of narrowband signals distorted by the Doppler shift in the order of multiples of the signal bandwidth. The description of the proposed algorithms includes an analytical approach of its development and, if possible, the analytical performance assessment. The algorithms are modeled in MATLAB Simulink and the models are used for validating the performance of the simulation. The models were also used for experimental tests on the real signal received from the PSAT satellite at the laboratory of experimental satellites at the department of radio electronics.

Abstrakt

Dizertační práce je zaměřena na softwarově definované přijímače určené k úzkopásmové družicové komunikaci. Komunikační kanály družicových spojů zahrnujících komunikaci s hlubokým vesmírem jsou zatíženy vysokými úrovněmi šumu, typicky modelovaného AWGN, a silným Dopplerovým posuvem signálu způsobeným mimořádnou rychlostí pohybu objektu. Dizertační práce představuje možné postupy řešení výpočetně efektivní digitální downkonverze úzkopásmových signálů a systému odhadu kmitočtu nosné úzkopásmových signálů zatížených Dopplerovým posuvem v řádu násobků šířky pásma signálu. Popis navrhovaných algoritmů zahrnuje analytický postup jejich vývoje a tam, kde je to možné, i analytické hodnocení jejich chování. Algoritmy jsou modelovány v prostředí MATLAB Simulink a tyto modely jsou využity pro ověření vlastností simulacemi. Modely byly také využity k experimentálním testům na reálném signálu přijatém z družice PSAT v laboratoři experimentálních družic na ústavu radioelektroniky.